SAKARYA UNIVERSITY
INSTITUTE OF NATURAL SCIENCES

SYNTHESIS AND CHARACTERIZATION OF Yb^{3+}-DOPED $Y_3Al_5O_{12}$ NANOCRYSTALS TO DEVELOP AN ABSOLUTE LUMINESCENT THERMOMETER

M.Sc. THESIS

Hossein EBRAHIM HOSSEINI TAZEH KANDI

Department : NANOSCIENCE AND NANOENGINEERING

Supervisor : Prof. Dr. Hatem AKBULUT

January 2018

SAKARYA UNIVERSITY
INSTITUTE OF NATURAL SCIENCES

SYNTHESIS AND CHARACTERIZATION OF Yb^{3+}-DOPED $Y_3Al_5O_{12}$ NANOCRYSTALS TO DEVELOP AN ABSOLUTE LUMINESCENT THERMOMETER

M.Sc. THESIS

Hossein EBRAHIM HOSSEINI TAZEH KANDI

Department : NANOSCIENCE AND NANOENGINEERING

This thesis has been accepted unanimously by the examination committee on 26.01.2018.

Prof. Dr. Hatem AKBULUT Head of Jury	Prof. Dr. Sefer Cem OKUMUŞ Jury Member	Doç. Dr. Hasan KOTAN Jury Member

DECLERATION

I anounce that all the information in this thesis was gotten by myself in academic rules, all visual and written information and results were displayed in understanding with scholarly and moral rules, there is no distortion in the presented data, in case of utilizing other people's works they were refereed legitimately to logical standards, the data demonstrated in this thesis has not been utilized in any other thesis in this university or in any other university.

Hossein EBRAHIM HOSSEINI TAZEH KANDI

26.01.2018

ACKNOWLEDGEMENTS

First of all, I express my truthful gratitude to Prof. Dr. Hatem AKBULUT, Prof. Dr. Sefer Cem Okumuş and Prof. Dr. Jordi Riu Rusell for giving me the opportunity to join the FiCMA-FiCNA group of the Departament de Química Física i Inorganica of the Universitat Rovira i Virgili in Tarragona in Spain that is advised by Dr. Maria Cinta Pujol Baiges and Dr. Joan Josep Carvajal Martí and develop this master thesis. Then, I aspire to utter my gratitude to Erasmus Programme and Erasmus+ that has been located in Sakarya University due to their financial supports along a research.

Furthermore, I would like to express my thankful for the technician and laboratory members of the FiCMA-FiCNA group such as Agusti Montero, Nicolette Bakker, and Gemma Marsal. I would like to extent my thanks to the some of the members of our group Prof. Dr. Francesc Díaz (group leader), Prof. Dr. Magdalena Aguiló, Josué Mena Gómez, Josep Maria Serres, Marc Medina Martínez, Oleksandr Savchuk, Eric Pedrol, Irina Adell Barbarà, Esrom Aschenaki Kifle, Nisrin Mohamed Bhiri, Jordi Aixart Forés, and Xuzhao Zhang. I also give my thanks to the technicians of the Servei de Recursos CientíficoTècnics of the URV (Dr. Francesc Gispert i Guirado and Rita Marimon Picó), who helped me a lot in my research.

At last, I would like to express my deeply gratefulness to my parents Ahmad Ebrahim Hosseini Tazeh Kandi and Roghayyeh Ghorbani Tazeh Kandi. You helped me when I was in trouble and dilemma when I was in Tarragona. I appreciate my dear sister, Zahra, my uncle, Hossein Ghorbani, and my step-uncle, Mustafa Tarakçı for your supporting in many ways by Skype, IMO, and Whatsapp calls. I would like to thank my landlord Mr. Carlos Arias, for providing me accommodation and peaceful stay during the study period in Tarragona, as well.

TABLE OF CONTENTS

LIST OF SYMBOLS AND ABBREVIATIONS

SYMBOLS

°	: Degree
%	: Percent Sign
$Al(NO_3)_3 \cdot 9H_2O$	: Aluminum Nitrate Nonahydrate
Al_2O_3	: Aluminium Oxide
$AlCl_3.6H_2O$	: Aluminum Chloride Hexahydrate
$C_{10}H_{16}N_2O_8$	: Ethylenediaminetetraacetic Acid
C_2H_6O	: Ethanol
$C_2H_6O_2$	: Ethylene Glycol
$C_6H_8O_7$	: Citric Acid
Cu	: Copper
h	: Hour
H_2O	: Distilled Water
HNO_3	: Nitric Acid
InGaAs	: Indium Gallium Arsenide
g	: Gram
K	: Kelvin
kV	: Kilovolt
K_α	: Cationic Radiation
mA	: Milliampere
mL	: Millilitre
nm	: Nanometre
RE_2O_3	: Rare-Earth Metal Oxides
s	: Second
µm	: Micrometer

$Y(NO_3)_3.6H_2O$	: Yttrium(III) Nitrate Hexahydrate
Y_2O_3	: Yttrium(III) Oxide
$Y_3Al_5O_{12}$	: Yttrium Aluminium Garnet
$Y_4Al_2O_9$	: Yttrium Aluminium Monoclinic
$YAlO_3$	: Yttrium Aluminium Perovskite
$YCl_3.6H_2O$	: Yttrium(III) Chloride Hydrate
$Yb(NO_3)_3 \cdot 5H_2O$	: Ytterbium(III) Nitrate Pentahydrate
Yb_2O_3	: Ytterbium(III) Oxide
$YbCl_3.6H_2O$	: Ytterbium(III) Chloride Hydrate

ABBREVIATIONS

CCD	: Charge Coupled Detector
CIF	: Crystallographic Information File
EDTA	: Ethylenediaminetetraacetic Acid
EG	: Ethylene Glycol
FIR	: Fluorescence Intensity Ratio
II-BW	: Second Biological Windows
JCPDS	: Joint Committee on Powder Diffraction Standards
PL	: Photoluminescence
RE	: Rare Earth
RT	: Room Temperature
TEM	: Transmission Electron Microscopy
UCNPs	: Upconversion Nanoparticles
XRD	: X-Ray Diffraction
YAG	: Yttrium Aluminium Garnet
YAM	: Yttrium Aluminium Monoclinic
YAP	: Yttrium Aluminium Perovskite

LIST OF FIGURES

LIST OF TABLES

SUMMARY

Keywords: Yb^{3+}, YAG, Luminescent, Nanothermometer, FIR, Biological Windows.

In this thesis, due to the great interest of the temperature measurements in the fields of nanomedicine and nanotechnology, the properties of Yb^{3+}-doped YAG (Yttrium Aluminum garnet, $Y_3Al_5O_{12}$) nanocrystals as an absolute luminescent nano-thermometer for biomedical applications was investigated. During the investigation, three routes of synthesis of Yb^{3+}:$Y_3Al_5O_{12}$ nanoparticles were done via the sol-gel modified Pechini method. Morphological and structural characterization approaches which include transmission electron microscope (TEM) and X-ray diffraction (XRD) were employed to optimize the process of the synthesis. Spectroscopic characterization techniques, such as absolute intensity technique which was applied for determining the most strongest emission intensity among the synthesized nanopowders using the integrated sphere and fluorescence intensity ratio (FIR) technique which was utilized to examine the temperature sensing capabilities of Yb^{3+}:YAG, were exploited. Thus, the best working performances of Yb^{3+}-doped YAG nanocrystals were detected.

The outcomes indicated that the highest absolute emission intensity was belong to 5 at. % of Yb^{3+}:YAG nanocrystals which were synthesized using nitrates as beginning materials and citric acid as a complexing agent viz Exp. 10. Under excitation at 940 nm and 980 nm, these nanoparticles exhibited emission bands at 1030, 1048, 1000, and 1006 nm within the range of the near-infrared (NIR) region, being in agreement with the $0' \rightarrow 2$, $0' \rightarrow 3$, $1' \rightarrow 3$, and $1' \rightarrow 2$ transitions of Yb^{3+}, and locating on the second biological windows (II-BW), correspondingly. Therefore, emissions from both of these excitations displayed favorable features in order to the thermic detecting within this scope of wavelengths. Ergo, two different thermometric parameters were defined as the ratios for both of the excitations, first, the ratio amongst the emission intensities of the $0' \rightarrow 2$ and $0' \rightarrow 3$ transitions being consistent with 1030 and 1048 nm peaks, second, the ratio betwixt the emission intensities of the $1' \rightarrow 3$ and $1' \rightarrow 2$ transitions concurring with 1000 and 1006 nm peaks. Thus, depending on the simple Yb^{3+} energy level structure, the thermometer was developed and could activate between 298 and 333 K. Computing capability of the calibration factor from the Yb^{3+} emission spectrum was the other novel and of greatest significance perspective.

Yb^{3+}:$Y_3Al_5O_{12}$ NANOKRİSTALLERİNİN MUTLAK BİR LÜMİNESANS TERMOMETRE GELİŞTİRMEK İÇİN SENTEZ VE KARAKTERİZASYONU

ÖZET

Anahtar kelimeler: Yb^{3+}, YAG, Lüminesans, Nanotermometre, FIR, Biyolojik Pencereler.

Mevcut yüksek lisans tez çalışmasında, nanotıp ve nanoteknoloji alanlarındaki sıcaklık ölçümlerine olan büyük ilgiden dolayı, Yb^{3+}:YAG (Yitriyum Alüminyum Granet, $Y_3Al_5O_{12}$) nanokristallerinin özellikleri biyomedikal uygulamalar için mutlak lüminsans bir nano-termometre olarak araştırılmıştır. Araştırma sırasında, Yb^{3+}:$Y_3Al_5O_{12}$ nanoparçacıklarının üç sentez yolu, sol-jel modifiye Pechini yöntemi ile yapılmıştır. Sentez prosedürünü optimize etmek için X-ray difraksiyon (XRD) ve geçirimli elektron mikroskobu (TEM) gibi yapısal ve morfolojik karakterizasyon teknikleri kullanılmıştır. Entegre küre kullanılarak sentezlenen nanoparçacıklar arasındaki en güçlü emisyon şiddetini belirlemek için uygulanan mutlak yoğunluk tekniği ve Yb^{3+}:YAG nanokristallerin sıcaklık algılama yeteneklerini incelemek için kullanılan floresans yoğunluk oranı (FIR) tekniği gibi spektroskopik karakterizasyon teknikleri kullanılmıştır. Böylece Yb^{3+}:YAG nanokristalleri için en iyi çalışma performansları belirlenmiştir.

Elde edilen sonuçlar, en yüksek ve güçlü mutlak emisyon şiddetinin % 5 Yb^{3+}:YAG nanokristallerine yani Exp. 10'a ait olduğunu ortaya koymaktadır ki, başlangıç materyalleri nitratlar olarak ve sitrik asit gibi bir kompleksleştirici ajan kullanılarak sentezlenmişlerdir. 940 nm ve 980 nm'de uyarma altında, bu nanopartiküllerin yakın kızılötesi bölge aralığında ikinci biyolojik pencerelerde (II-BW) bulunan 1030, 1048, 1000 ve 1006 nm'de emisyon bantlarının sırasıyla $0' \rightarrow 2$, $0' \rightarrow 3$, $1' \rightarrow 3$ ve $1' \rightarrow 2$ İterbiyum geçişlerine karşılık gelmesi gösterilmiştir. Bu nedenle, bu uyarımların her ikisinden de gelen emisyonlar, bu dalga boyu aralığında termal algılama için umut verici özellikler sergilemektedir. Dolayısıyla, her iki uyarımın oranları olarak iki farklı termometrik parametre belirlenmiştir, birincisi, 1030 ve 1048 nm piklerine karşılık gelen $0' \rightarrow 2$ ve $0' \rightarrow 3$ geçişlerinin emisyon şiddetleri arasındaki oran, ikincisi, 1000 ve 1006 nm piklerine karşılık gelen $1' \rightarrow 3$ ve $1' \rightarrow 2$ geçişlerinin emisyon şiddetleri arasındaki orandır. Termometre, basit Yb^{3+} enerji seviyesi yapısına dayalı ve 298 ile 333 K arasında çalışabilmektedir. Diğer yeni ve en önemli özellik, kalibrasyon faktörünün Yb^{3+} emisyon spektrumundan hesaplanabilmesidir.

CHAPTER 1. INTRODUCTION

First of all, we need to know what is the heat and temperature? These two amounts are identified with each other however, they are unique. Heat is the energy that is exchanged starting with one body then onto the next because of temperature contrast among the two bodies and utilization of two common units for it, viz calorie and joule, are found [1].

As has been noted above, heat and temperature are different quantities but they are closely related to each other. There are different definitions for temperature. Herein, we notify three of them;

a. The temperature of a matter is its level of hotness or coldness [1].
b. The temperature of a matter is an index of the mean thermal energy (kinetic energy) of the molecules of the matter [1].
c. Once two matters at various temperature are gotten contact, heat streams from a matter at a higher temperature to the matter at lower temperature till the temperature of the two matters are the equal. Afterwards, the temperature of the two matters chooses the direction of heat stream when the two matters are acquired contact [1].

There several units for temperature which are Celsius, Fahrenheit, Reaumer, and Kelvin or absolute temperature [1-2].

Nowadays, temperature as a major thermodynamic factor assumes a critical part in our life, especially in science [3]. Therefore, its measurement is a subject of incredible enthusiasm for some areas. Climate and marine research, metrology, aerodynamics, chemistry, biology, medicine, military innovation, ventilating, whole apparatuses for

generation plants and the storage of food, warming and cooling, and different merchandise are a portion of the bigger regions which are relied upon the temperature [3]. Thus, it is assessed that the quota of sensors for temperature quantities approximately 75%–80% of the global sensor bazaar [3]. The greater part of these sensors need straight contact with the matter, which are known as contact thermometers, utilizing the heat exchange and are hence futile for exact temperature estimations at the below micron range, for instance, in semiconductor intersections in microelectronics and intracellular mappings in nanomedicine [4].

At the present time, nanoscience and nanotechnology as a new field of research and development in many fields such as medicine, electronics, metallurgy and material science, chemistry, biology, mechanics optoelectronics, and etc. is the most rapidly advancing technology. Non-contact thermometers as one of these advancements, in which there isn't expected to contact with the quantifiable object and the temperature perusing are done through various temperature subordinate properties of an object, is been happening in thermometer fields. Thus, a certain framework temperature with the spatial resolution of below micrometric has become feasible to quantify with them. This has prompted the advancement of another subfield of thermometry called nanothermometry, pertaining to the temperature estimation at the nanoscale level.

With regards to the nanoscale applications, nanothermomerty procedures can be sorted as non-luminescent and luminescent thermometers [5]. According to the non-luminescent systems, thermometric properties are not straightforwardly identified with luminescence. Some of the well-known methods of non-luminescent temperature measurements including scanning thermal microscopy, nanolithography, carbon nanotube, and biomolecular thermometries have been developed up to now for nanoscale applications [5]. Pursuant to luminescent thermometers, they exploit light to measure temperature. IR thermography, optical interferometry, thermoreflectance, Raman spectroscopy, and luminescence are the most common ones which are found in literature [5].

In the following chapter, we will start with the most fascinating ones of the luminescent thermometers which are the luminescence nanothermometries due to their benefits in numerous high-tech utilizations in an expansive assortment of zones, for example, microfluidics, microelectronics, bio- and nanomedicine, and additionally being a significantly more solid approach in order to the exact temperature estimations, and also the different types of them will be briefly explained. Next, we will focus our main attention on band-shape types of the luminescence nanothermometry exploiting the fluorescence intensity ratio (FIR) theory. Later, the host material which are used in this thesis will be described. Finally, the chapter will end with the objectives of this thesis.

1.1. Luminescence Nanothermometry

Luminescence is the reverse procedure to absorption. Generally, happening of the emission of light from a given object is called luminescence, which means an external excitation source (absorption of one or more photons in the case of photoluminescence) makes the luminescent molecule energy to jump to higher electronic states and from where it will be emitted in the form of light or heat, reverting back to the ground state or to an intermediate state [6]. This procedure is schematically outlined in the Jablonski energy level diagram in Figure 1.1. [7].

The emitted photons features rely upon the electronic states features engaged with photon emanation, which, in turn, rely upon the local temperature of the system [8]. Therefore, it can be understood that luminescence nanothermometry utilizes the connection amongst the features of temperature and luminescence for accomplishing thermic detecting via the spatial and spectral investigation of the light created by the substance to be thermally depicted [8].

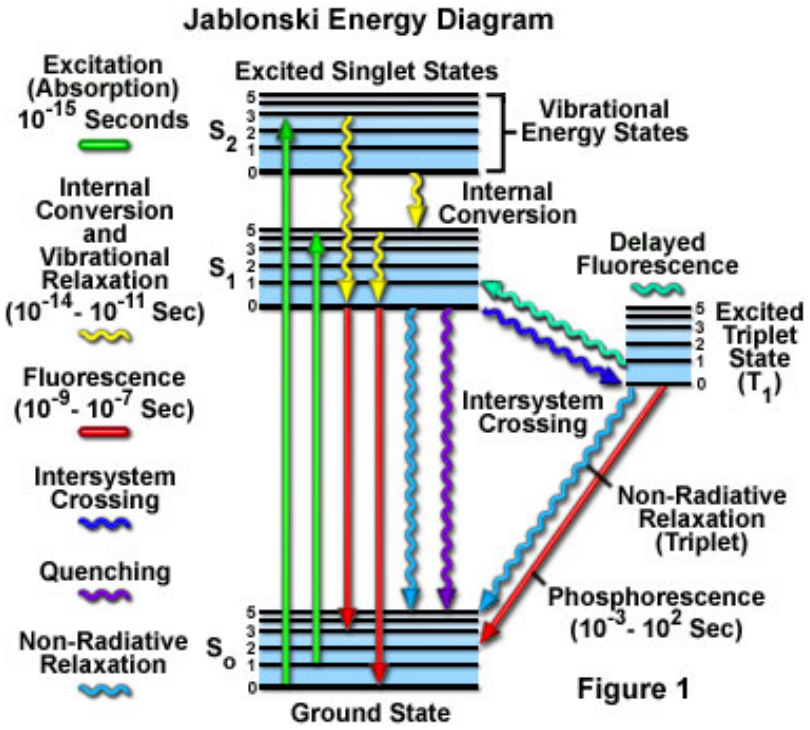

Figure 1.1. Illustration of the luminescence process by Jablonski energy level diagram [7].

Luminescence thermometry in the visible and near-infrared (NIR) which demonstrates high spatial, thermal and temporal resolution, high stability, a large measurement range, acceptable cost and size, is one of the most promising non-contact techniques for temperature determination. This nanothermometry in terms of the specific parameter of luminescence can be classified in six routes [8]. These parameters are analyzed and then the calculation of thermic reading is obtained [8]. Figure 1.2. schematically displays these various parameters which describe a given substance luminescence emission: intensity, band-shape, spectral position, polarization, lifetime, and bandwidth [8]. Therefore, considering these alterations, the description of the six sub-classes luminescence nanothermometry is feasible which include Intensity-based Nanothermometry (INth), Band-Shape-based Nanothermometry (BSNth), Spectral-baesd Nanothermometry (SNth), Polarization-based Nanothermometry (PNth), Bandwidth-based Nanothermometry (BNth), and Lifetime-based Nanothermometry (LNth) [8]. These models of luminescence thermometers will briefly explain in the next sub-sections.

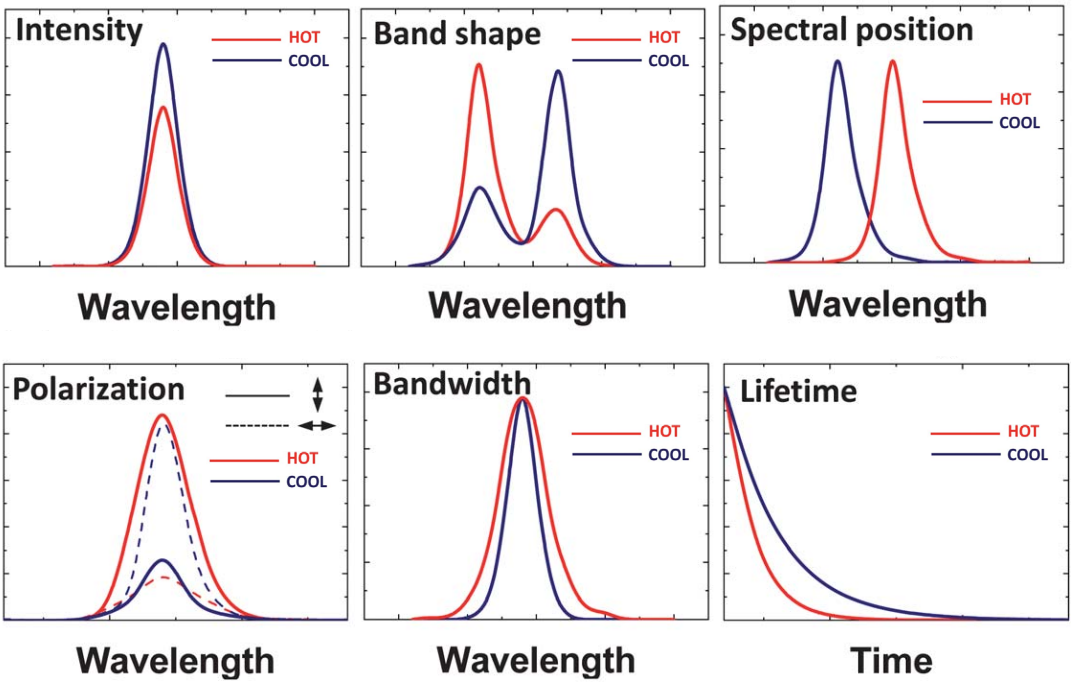

Figure 1.2. Schematic portrayal of the conceivable influences made through a temperature increase on the luminescence. The higher temperatures have been indicated by the red lines [8].

1.1.1. Intensity-based nanothermometry (INth)

For this situation, thermic detecting is accomplished via the luminescence intensity investigation or in the other words the variation of the temperature yields in the alteration of one of emitting band intensity. At the point when temperature varies, there is a general alteration in the quantity of emitted photons every second with the end goal in which the spectrum of the emission gets to be less (or increasingly) intense. The thermic activity of luminescence quenching mechanisms and additionally increments within the possibilities of the non-radiative decay are the common cause of the temperature induced variations in the intensity of the luminescence [8].

The principle favourable position of such thermometer is simplicity. The application of it is somewhat not popular because of its low accuracy. Whereas the intensity of emission band may rely upon many elements such as the measure of phosphor utilized, absorption or scattering and so on, the estimation of temperature is fairly unsafe and its exactness is low [9]. These kind of the nanothermometers has been reported in the

five systems, containing polymer-based, nanogel-based, Rare earth-based, Dye-based, and QD-based systems.

1.1.2. Band-Shape-based nanothermometry (BSNth)

The most common is the subclass of luminescence nanothermometers in view of the examination of relative fluorescence intensity amongst the diverse emission bands according to the appropriate transitions [10]. It is well-known band-shape luminescence nanothermometry and will be discussed in the next section. The relative intensity amongst the diverse spectral lines which construct the luminescence spectra is well-known as the phrase “band-shape”. The strong dependence of this relative intensity to the temperature is obvious, as well. Once the electronic states from which emission is produced are nearby in energy such that they are thermally joined, thermally caused changes in the band-shape typically happen [8]. It is often referred to as ratiometric sensing which we will use in this research and will be discussed in the 1.2. subsection of this chapter.

There are two models of operation schemes for band-shape nanothermometry: (i) Once the luminescence bands/lines are created via various emitting centres, (ii) Once the luminescence bands/lines are created via a single luminescent centre [8]. In the first model, the temperature caused variations within the band-shape of the framework arise from the various thermal quenching ratio of every centre or through thermally caused variations in the energy transfer rates between these emitting centres [8]. According to the second model, the alterations in the band shape of the system are commonly created via a thermally induced population re-distribution between the various energy levels of the emitting center [8]. It should be noted that, in both cases, the luminescence bands/lines relative intensity relies just upon temperature. Therefore, the principle favorable position of this procedure over intensity-based nanothermometry is that the thermal perusing isn’t influenced by fluctuations in the luminescence centers focuses [8]. An extraordinary assortment of these nanothermometers has been accounted for in the literature which can be categorized in three different systems including QD-based, Rare earth-based, and Dye-based systems [8].

1.1.3. Spectral-based nanothermometry (SNth)

The spectral thermometers are characterized by the variations of the position of emission bands with temperature which are clearly distinguished using the energy separation among the two electronic levels associated with the emission. It relies upon the refractive index and inter-atomic distances (density) as two of the great assortment of temperature subordinate factors of the emitting matter. The fundamental preponderance of this method is that temperature perusing is not influenced via the fluctuations of the luminescence intensity made via changes in the nearby concentration of the emitting centers, fluctuations of the energy of the excitation source, shading impacts or movements. According to the literature, in spite of the fact that the attendance of temperature induced spectral shifts has been discovered within numerous luminescent frameworks, however, the semiconductor QDs are the only matters which are effectively utilized as a high-resolution SNth [8].

1.1.4. Polarization-based nanothermometry (PNth)

At the anisotropic medium, this kind of the nanothermometry relies upon the temperature effects on the polarization anisotropy parameter. The mentioned parameter is defined as a proportion from the emitted of luminescence intensities at two orthogonal polarization states which is written as the following equation [8];

$$r = (I_{\parallel} - I_{\perp})/(I_{\parallel} + 2I_{\perp}) \quad (1.1)$$

wherein $I_{\parallel}$ is the intensities of the luminescence polarized parallel and $I_{\perp}$ is the intensities of the luminescence polarized perpendicular to the incident polarization. As an example, Fluorescein molecules are one of them which were employed on the previous periods for this sort of thermometry [8].

1.1.5. Bandwidth-based nanothermometry (BNth)

The luminescence-spectra bandwidth alteration is used within this nanothermometry to accomplish a thermic detecting. The different-emission lines' width which produces every luminescence spectra is specified via the features of the temperature and material. When the luminescent material temperature is expanded, an increment within the density of phonons happens, correspondingly, yielding through the spectral share of uniform line widening. For the most part, at room temperature proximity, uniform line widening prompts a linear correlation amongst temperature and data bandwidth [8].

In terms of greatness, the temperature prompted luminescence line widening is generally little which is a fundamental impediment to this strategy. Therefore, it can be just found within frameworks which demonstrate the intrinsic narrow emission lines and also, in turn, the inhomogeneous line widening is not overcome of uniform one, e.g., combining of rare-earth (RE) ions at several crystalline hosts. As a standout related instance, it can be noted the case of Nd^{3+} ions within the common YAG host (Nd:YAG) [8].

1.1.6. Lifetime-based nanothermometry (LNth)

The effect of the temperature on lifetimes of the excited states is utilized for temperature determination in lifetime luminescence thermometers. The description of the luminescence lifetime, τ_f, is the time in which the intensity of the emitted luminescence degrades down into 1/e of its first amount behind a pulsed excitation which is a complete-decay-possibility indication of the emitted intensity. Since decay possibilities from electronic levels rely upon an extraordinary assortment of parameters and a significant number of them are identified with temperature, (for instance, phonon-assisted energy transfer processes and multiphonon decays), the value of their excited state decay times may be taken into account as a temperature sensor [8]. This kind of the nanothermometer has been developed in a various systems

which can be grouped into four various classifications including rare earth ions, quantum dots, luminescent dyes, polymers or membranes.

1.2. Fluorescence Intensity Ratio (FIR) Theory

By a reasonable pump source, a framework experiencing steady excitation is assumed. In such system, the specific energy level which is attentiveness, the host material, the technique of the excitation, and as well as the ion-doped material dimensions utilized are various factors that rely on the intensity of emission from a particular energy level of a group of ions doped in a host matrix. Because of the temperature reliance of nonradiactive rates of the energy level of interest or, in a few conditions, from another energy levels of the ion, temperature-related variations in the intensity of the emission generally, emerge. In this way, by evaluating the intensity of emission beginning from a specific level, the temperature could be deduced. In such framework, every adjustment within the intensity of the excitation or within transmission misfortunes within guiding fibers, anyway, would be translated inaccurately as alterations in temperature. The gauge of the fluorescence intensity through two distinctive energy levels having diverse temperature conditions is a method for dodging of this issue, the yielding proportion gives a measure with basically free from fluctuations in the intensity of the excitation and twist losses [11].

An exceptional instance of the FIR estimation strategy includes using the intensities of the fluorescence through two nearly spaced energy levels for temperature gauging. Due to the emitted intensities are proportionate to every energy level population, the proportion of the emission intensity from two thermally paired energy levels is the FIR which can be defined by [11];

$$\mathrm{FIR} = \frac{N_2}{N_1} = \frac{I_{2j}}{I_{1j}} = \frac{g_{2j}\sigma_{2j}\omega_{2j}}{g_{1j}\sigma_{1j}\omega_{1j}} \exp\left(\frac{-\Delta E}{kT}\right) \implies \mathrm{FIR} = A \,.\, \exp\left(\frac{-\Delta E}{kT}\right) \qquad (1.2)$$

Herein, the FIR from two thermally paired energy levels pursues a Boltzmann type population distribution. Where I_{ij} is the fluorescence intensity, g_i is the degeneracy of

levels, ω_{ij} is the emission cross-section and the angular frequency of fluorescence transitions from the upper (i = 2) and lower (i = 1) thermalizing energy levels to a terminal level j, ΔE is the energy difference between the two thermally paired levels, k is the Boltzmann constant, T is the absolute temperature, and $A = (g_{2j}\sigma_{2j}\omega_{2j}) / (g_{1j}\sigma_{1j}\omega_{1j})$. The exploited energy levels for the fluorescence intensity ratio has been shown in the Figure 1.3.

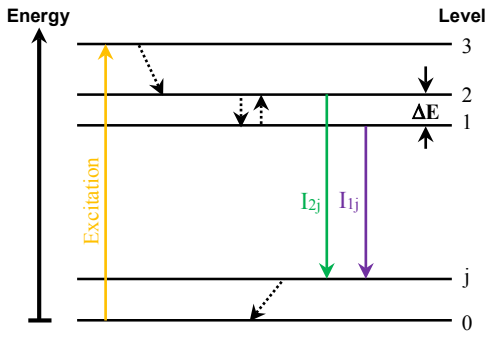

Figure 1.3. Presentation of the energy levels and transitions of interest via streamlined energy level chart for a conceivable case in which the FIR strategy can be utilized to detect temperature. The solid arrows pertinent to the fluorescence transitions employed for computing the FIR, while dashed lines relate to the decay of the non-radiative processes [11].

The thermally paired levels utilization in the FIR technique has a few points of interest over the utilization of two single levels. In the first place, the hypothesis of the relative variations in the fluorescence intensity is generally surely comprehended and in this way the conduct is simpler to anticipate. Secondly, the single thermally paired levels population is straightforwardly relative to the whole population. In this way, each adjustment within the aggregate population because of variation in excitation energy, e.g., will influence the single levels to a similar degree. It aids to decrease the reliance of the estimation procedure on the excitation energy, critical for sensor stability. At last, the emission wavelengths will be comparatively near which is implied via the moderately nearly divided energy levels utilization. This lessens any wavelength subordinate impacts because of fiber twists on the estimation [11].

For detecting applications, it is vital to know the rate at which the FIR variations for a little alteration in temperature. This amount, known as absolute sensitivity, can be computed from the primary derivative of FIR concerning the temperature;

$$S_{abs} = \frac{dFIR}{dT} = A \cdot \left(\exp\left(\frac{-\Delta E}{kT}\right)\right) \cdot \left(\frac{d(-\Delta E/kT)}{dT}\right)$$

$$\Rightarrow S_{abs} = A \cdot \left(\exp\left(\frac{-\Delta E}{kT}\right)\right) \cdot \left(\frac{\Delta E}{kT^2}\right) \quad (1.3)$$

To comfort the quantitative examination among the diverse ratiometric optical temperature sensors working by various components, the utilization of the relative sensitivity has been suggested [11];

$$S_{rel} = \frac{S_{abs}}{FIR} = \frac{A \cdot \left(\exp\left(\frac{-\Delta E}{kT}\right)\right) \cdot \left(\frac{\Delta E}{kT^2}\right)}{A \cdot \exp\left(\frac{-\Delta E}{kT}\right)}$$

$$\Rightarrow S_{rel} = \frac{\Delta E}{kT^2} = \frac{\Delta E}{kT^2} \times 100 \quad [\%.K^{-1}] \quad (1.4)$$

From the equations of (1.2) and (1.3), clearly, by utilizing a couple of energy levels with a greater energy diversity the FIR affectability would increment. Nevertheless, this is genuine to a limited restrain, in the event that the energy gap among them is too enormous, the thermalization would not be watched. Moreover, whenever the energy difference expands, the population together with the intensity of the fluorescence from the upper thermalizing level will diminish which is conceivable to indicate useful issues in attempting to quantify low light levels [11].

1.3. The Most Common Materials For Luminescence Nanothemometry

The nanotechnology's fast advancement has caused it conceivable to manufacture an assortment of photostable and strong nanometric fluorescent combinations with the typical size approxi-mately 100 nm. The little size of these nanoparticles (considerably smaller than the ordinary cell sizes) and the chemical functionalization of their surfaces have given a chance to join them effectively in living cells and to have a good possibility for luminescence mapping in vitro experiments. Subsequently, these nanoparticles whose fluorescence is sensitive to little temperature alterations in the

physiological range are conceivably valuable as nanothermometers, giving the feasibility of intracellular thermal mapping [12].

The several sorts of luminescent nanothermometers with the incredible possibility for pragmatic applications developed up to now including QDs, organic dyes, luminescent polymers, and lanthanide-doped nanoparticles.

1.3.1. Quantum dots (QDs)

Quantum dots or semiconductor nanocrystals are 1–10 nm inorganic tiny particles or nanocrystals with extraordinary size-subordinate optical and electrical features because of quantum confinement which were first found in 1980 by Ekimov et al. [13-15]. QDs are employed in various bio-medical applications like medical imaging, biosensors, etc. due to the unique optical feautres such as size-tunable absorption and emission frequencies, high quantum yield, and photostability [16-17].

According to the literature, QDs are presented in four forms of the previously mentioned parameters of the luminescence thermometers which are intensity, band-shape, spectral, and lifetime factors. There have been lots of studies try to develop the nanothermometer using these factors [18-22]. However, a few factors still block the utilization of economically accessible QDs at nanoscale thermometry, especially the bleaching, the bluing, and the twinkling beneath the consistent illumination [23-25], the QDs size dispensation which prompts a non-homogeneous luminescence singular reaction. From the other disadvantages can be noted the agglutination, the instability in various conditions, the weak solvency, and the toxicity to biologic frameworks [26-27].

1.3.2. Organic dyes

Dyes are aromatic organic compounds can, for the most part, be depicted as hued substances that have affinity to the substrates to which they are being employed and they are a critical class of synthetic organic compounds utilized as a part of numerous

industries, particularly textiles [28]. The primary synthetic dye, Mauveine, got from aniline, was found by Perkin in 1856 [29] and, from that point forward, the synthesis of organic dyes has been seriously studied and were licensed in 1941 as temperature pointers. The exceptionally famous ones out of an organic setting including RhB [30], fluorescein isothiocyanates [31], and cyanine dyes [32].

Dyes can be found in intensity, band-shape, and lifetime luminescence nanothermometers. Although an awesome assortment of cases within the literature have been reported using these materials [33-37], photobleaching as the fundamental restriction of the dye-based thermometers is blocked continuous long-term temperature estimation.

1.3.3. Polymers

Once numerous molecules of a basic compound consolidate, the item is named a polymer and the procedure is polymerization. The basic compounds whose atoms combine to shape the polymers are named monomers. The polymer is a chain of atoms, giving a spine, to which atoms or ensembles of atoms are attached [38]. The first observation of the alteration of the fluorescence emission of polymers with temperature is not obvious, however to the best of our insight, J. Yang et al., who demonstrated the temperature reliance of fluorescence of stepping ladder-like polyphenylsilsesquioxane (LPPS) and ladder-like 1.4-phenylene-bridged polyvinylsiloxane (LPPVS), was the earliest investigation [39]. According to literature, these materials have been reported in two forms of nanothermometers which are intensity and lifetime due to higher sensitivities of them and the design of them as the compatible in biologic beads has a key significance for in vivo usages [40-43].

Concerning these thermometers, the typical drawback is hysteretic phase transitions which are differences in the outcome for the same temperature value, based on whether the temperature is expanding or reducing and also for the situation that the optical reaction relies upon the nearby chemical condition, a conceivable non-uniform reaction over the polymer-bead is the other disadvantage [44].

1.3.4. Lanthanide (Ln^{3+})-doped nanoparticles

The fifteen lanthanide (Ln) arrangement (from lanthanum to lutetium) and additionally yttrium and scandium are known as rare earth elements. With the exception of La^{3+} and Lu^{3+}, the whole Ln^{3+} ions show distinguished luminescence features through intra-4f or 4f – 5d transitions because of plenty and inimitable energy level structures emerging through $4f^n$ internal shell configurations [45]. Their emissions become visible as slender spectral lines and their luminescence lifetime are moderately long (from µs to ms), once combined in a material and the intensity of these lines relys on several parameters among which, temperature is the most important one [46].

The observation of the abundant examples using these materials within the literature of luminescence nanothermometry is obvious which can be categorized in intensity [47], band-shape including single-center Ln^{3+}-UCNPs [48] and multi-center Ln^{3+}-UCNPs [49], bandwidth [50], and lifetime [51] models.

Specifically noteworthy are those Ln^{3+}-doped luminescent thermometers in view of upconversion nanoparticles (UCNPs) which assimilate light in the NIR area of the electromagnetic spectrum, and emit light in the visible range [52]. Therefore, the phrase upconversion (UC) correlates to an impact by which the change of the low-energy near-infrared (NIR) radiation to the higher energy (visible) light via (consecutive) multi-photon NIR absorption is occurred and the emission of shorter wave luminescence is resulted and also can be happened in singly or multiply doped host matrices. This phenomenon are appeared in Figure 1.4. [53].

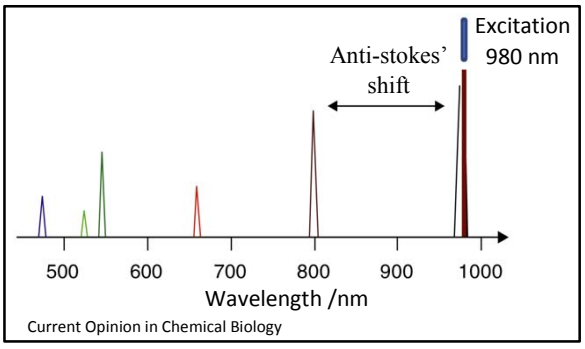

Figure 1.4. The plot of the upconversion impact. Excitation in the NIR at normally 980 nm prompts a few radiance emissions in the visible. The colors of the emission rely upon the dopant particles utilized [53].

As the advantages of these nanoparticles, it can be noted that they do not bleach and blink unlike QDs and their peak emission wavelength are not size-reliance, the NIR diode lasers employed to excite these UCNPs are cheaper and more powerful than the UV lasers [53].

Yb^{3+} ion one of these UCNPs is our interest in this research because of its simplest energy-level construction. It has only two electronic states which are $^2F_{7/2}$ ground state, and $^2F_{5/2}$ excited state and these two state are separated by approximately 10,000 cm^{-1} [54-55]. Reinberg et al. were the first to utilize a narrow band source to pump Yb ions [56]. Therefore, due to this simple electronic structure, the following advantages can be extacted [55, 57-58];

a. Utilization probability of Yb^{3+} as sensitizer ion for the other rare earth ions,
b. The non-existence of the excited state absorption, cross-relaxation process, more up-conversion, or any internal mechanism capable to diminish the impressive laser cross-section,
c. The intense and broad Yb^{3+} absorption lines are well suited for IR InGaAs diode laser pumping between 900 and 980 nm,
d. The broad emission band allows the generation of ultrashort pulses,
e. The non-existence of absorption within the visible range,
f. A small quantum defect between the absorption and emission wavelengths leads to a low thermal load (11% relative to 30–40% in Nd^{3+}-doped laser hosts).

1.4. Host Material Used In This Thesis

Of the garnet group, yttrium aluminium garnet (YAG, $Y_3Al_5O_{12}$) can be named as a synthetic crystalline material [59]. It is very well known compound, broadly connected as a strong host matrix for luminescent particles since it doesn't harm effectively under irradiance with an electron beam [60]. Extraordinary traits like great thermal and chemical stability, a high thermal conductivity has been made it as a great compound which generally utilized in different solid-state laser [61]. Properties such as the low creep rate, high oxidation resistance, and low electrical conductivity make it as an

encouraging high-temperature engineering material in order to insulation or refractory [60]. It additionlly has a big energy gap (6.5eV) which makes this material as an acceptable electric insulator [61].

The YAG crystal which can be written as $Y_3Al_2Al_3O_{12}$ in agreement with the general structural formula of garnet, belongs to the cubic crystal system with point group $m\bar{3}m$ and space group $la\bar{3}d$ [62]. However, there are different notations for this crystal system for each group (see Table 1.1. and Table 1.2.) [63-64]. The 3-Dimensional structure of YAG has been drawn in Figure 1.5a using the VESTA software and the crystallographic information file (CIF) of YAG (CIF given in Annex A) [65]. The structural data of YAG which are abridged in Table 1.3. by Nakatsuka et al. in 1999 [62]. The cubic space symmetry of this host matrix has eight formula units per unit cell as potrayed in Figure 1.5b. The **c** sites in the crystal are occupy by yttrium ions, Y^{3+}, which have **D_2** local symmetry. The aluminum ions, Al^{3+}, have two various sites, **a** and **d**, within the crystal. The aluminum ions at **a**-site experience the crystal field of **C_{3i}** symmetry, and the aluminum ions at **d**-site experience a crystal field of **S_4** symmetry [66]. Once the Yb^{3+} is doped in the YAG, it replaces with the Y^{3+} ions which are in dodecahedral sites and experience the same **D_2** local symmetry.

Table 1.1. Different notations of point group for the cubic system [63].

Point Group							
Crystal system	Hermann-Mauguin (full)	Hermann-Mauguin (short)	Shubnikov	Schoenflies	Orbifold	Coxeter	Order
Cubic	$\frac{4}{m}\bar{3}\frac{2}{m}$	$m\bar{3}m$	$\tilde{6}/_4$	O_h	*432	[4,3]	48

Table 1.2. Different notations of space group for the cubic system [64].

Space Group						
Crystal system	Short name	Full name	Schoenflies	Fedorov	Shubnikov	Fibrifold
Cubic	$la\bar{3}d$	$I\ 4_1/a\ \bar{3}\ 2/d$	O_h^{10}	99a	$\left(\frac{a+b+c}{2}/a{:}a{:}a\right){:}4_1//\tilde{6}.\frac{1}{2}\widetilde{abc}$	$8^0/4$

Table 1.3. Atomic coordinates (x,y,z) and Site Occupance Fraction (SOF) for YAG [65].

Atom	Wyckoff	x	y	z	SOF
Y	24c	0.125	0	0.25	1.00
Al1	16a	0	0	0	1.00
Al2	24d	0.375	0	0.25	1.00
O	96h	-0.0318 (3)	0.0511 (3)	0.1498 (3)	1.00

Note: Space: $la\bar{3}d$, Lattice constant: $a_0 = 12.0062(5)$ Å , $Z = 8$
Bond lengths: $Y - O: 2.317Å \times 4, Y - O: 2.437Å \times 4, Al1 - O: 1.938Å \times 6, Al2 - O: 1.754Å \times 4.$

YAP ($YAlO_3$), YAM ($Y_4Al_2O_9$), and YAG ($Y_3Al_5O_{12}$) are the three permanent phases the yttria-alumina system, i.e., the formation of YAP and YAM phases as intermediate outgrowths is possible even if the synthesis of YAG is done by stoichiometric admixture of Y_2O_3 and Al_2O_3. Thus, to shape a pure garnet phase, wide heat treatments at high temperature (>1600C) and repetitious mechanical milling needed for decomposition of the intermediates [60].

Polymerized complex manner, metal-organic preceramic procedure, co-precipitation processes or yttrium carboxylate-alumoxane way are some of the wet-chemical methods have been exploited to generate YAG phases. The complexing and expending (long refluxing time, gelation periods of few days, etc.) procedures and the discrepancy in the solution behavior of various chemical species are the disadvantages of the noted methods. In addition to these, because of the phase division trends of unimetal phases, an exact control of cationic stoichiometry is not gained [60].

In general, according to the ordinary stategies which have been utilized in order to prepare the doped materials where a few atomic weight rate of a constituent is to be homogeneously scattered in a doped material, non-identical blending, remaining phases, unreacted onset materials are the main challenges. Therefore, the best options due to their chemical cross-connecting of various metal centers within the original blend from precursor sorts causing a homogeneous distribution of dopant ions in an identity matrix are the sol-gel methods dependent on the molecular precursors [60]. The pioneering works of Veith et al. [67] are the representative examples of this method, who used this method for synthesizing the undoped YAG and Ce-doped YAG ceramics, Wang et al. [68], who employed for producing the Yb-doped YAG

nanopowders and thin films of them at nano scale, Garskaite et al. [69], who utilized to prepare a YAG powders and thin films deposited on silicon substrates.

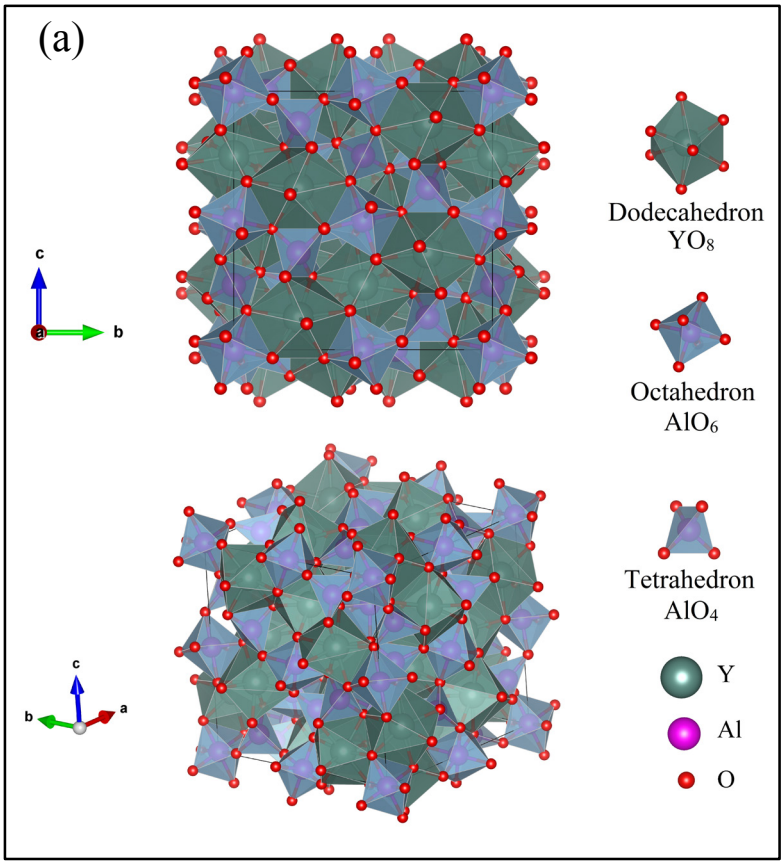

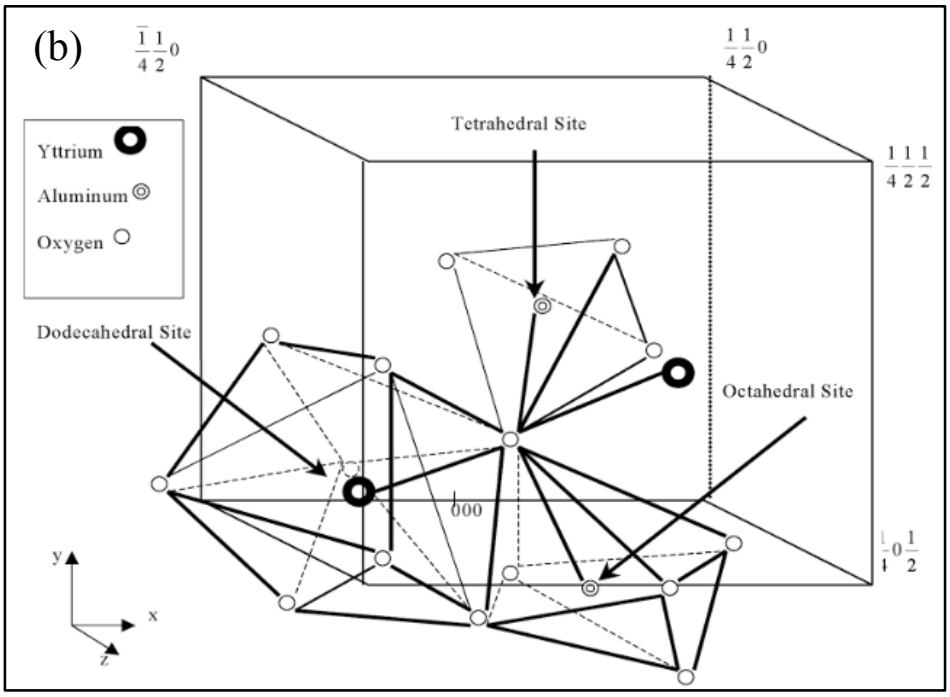

Figure 1.5. (a) The YAG crystal structure with three various cation-oxygen polyhedral inside the garnet structure. (b) One octant of the unit cell of YAG lattice [66].

1.5. Aim Of This Thesis

The goal of this work is to study the temperature dependence of the luminescence properties of optically active Yb^{3+} ions in the YAG as a host matrix and to explore the use of Yb^{3+}-doped YAG nanocrystals as an absolute luminescent nano-thermometer that not requires previous calibration for biomedical applications. In order to do this, we exploited two types of the well-known spectroscopic characterization techniques which were absolute intensity and fluorescence intensity ratio (FIR).

The modified Pechini method has been used for synthesizing these nanocrystals and in collaboration with the Física i Cristal•lografia de Materials i Nanomaterials (FiCMA-FiCNA) group of the Departament de Química Física i Inorganica of the Universitat Rovira i Virgili in Tarragona in Spain.

CHAPTER 2. EXPERIMENTAL TECHNIQUES

2.1. Sol-Gel Synthesis: The Modified Pechini Method

The sol-gel synthesis method was developed in the 1960s and allowed to synthesize nanoscale materials with a high-purity and high-homogeneity at lower temperatures [70]. In common, it comprises of the taking after five steps [71];

a. Sol development which is the name of a colloidal solution made of solid particles, a few hundred nm in diameter, suspended in a fluid phase.
b. Gelling which is a solid macromolecule immersed in a solvent.
c. Shape forming
d. Drying
e. Densification.

In 1967, a modification of sol-gel method to get ready lead and alkaline earth titanates and niobates by utilizing resin intermediates was proposed by Maggio P. Pechini [72-73]. Before all else, the shaping of a blend of cations is done in ethylene glycol solution and an organic complexing agent, CA, (citric acid or ethylenediaminetetraacetic acid, EDTA). At the second step, turning the cations into a chelate and the polymeric resinate shapes are happen. At last, the polymer is disintegrated at 573 K. Thus, this method is included two reactions which are a complex formation betwixt metals and citric acid or EDTA, and a sterification betwixt ethylene glycol (EG) and citric acid or EDTA. To decrease every isolation of the cations is the goal of the polymeric natural net via sterification [73]. After that time, this modification of the sol-gel method has been known as the modified Pechini method. As an example, it is a helpful procedure for preparation of highly dispersed metal oxides, with homogeneous blending of the

beginning materials at the atomic level gel, low manufactured temperature, great control of stoichiometry, fine particle size, and uniform morphology [74].

The advanced methods by Galceran et al. [73] were pursued to generate Yb^{3+}:YAG nanoparticles through the sol-gel modified Pechini method. In general, three routes of synthesis of Yb^{3+}:$Y_3Al_5O_{12}$ nanoparticles were done. Flowcharts of these three routes of the procedure to generate the Yb^{3+}:YAG utilizing the modified Pechini method are portrayed in Figure 2.1. and Figure 2.2.

For clarification the modified Pechini method, experimental pictures for preparation of the Yb^{3+}:YAG nanocrystals using Y_2O_3 (Aldrich, 99.99%), Yb_2O_3 (Alfa Aesar, 99%), and Al_2O_3 (Merck, γ-Tonerde) as starting materials preparation is presented in Figure 2.3. and Figure 2.4., as well.

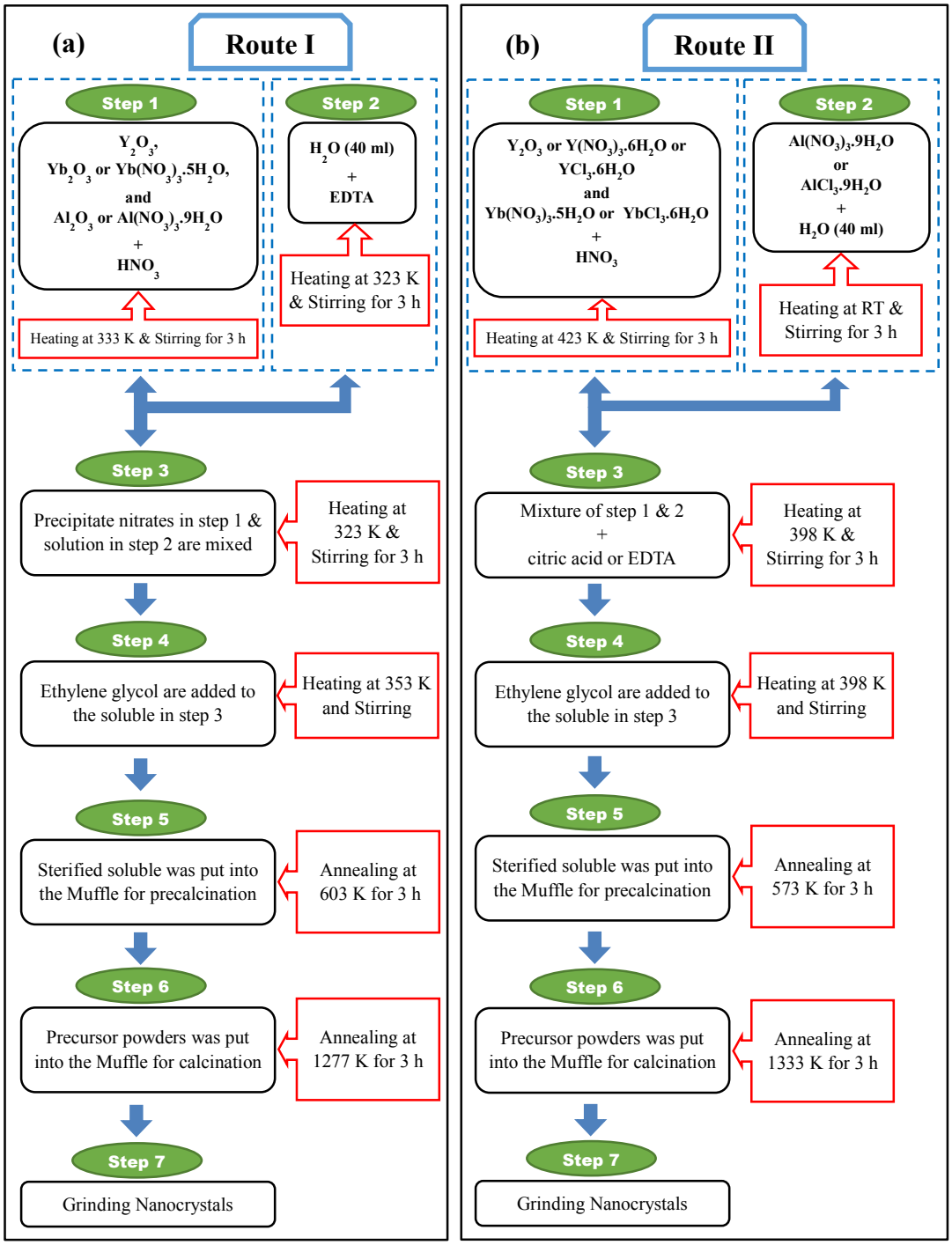

Figure 2.1. Flowchart of the modified Pechini method for Yb^{3+}-doped YAG nanocrystals synthesis in three different route. (a) Route I: The prepared nanoparticles from Exp. 01 to Exp. 06 were done by this type of synthesis, (b) Route II: The prepared nanoparticles from Exp. 07 to Exp. 20 and from Exp. 41 to Exp.48 were done by this type of synthesis.

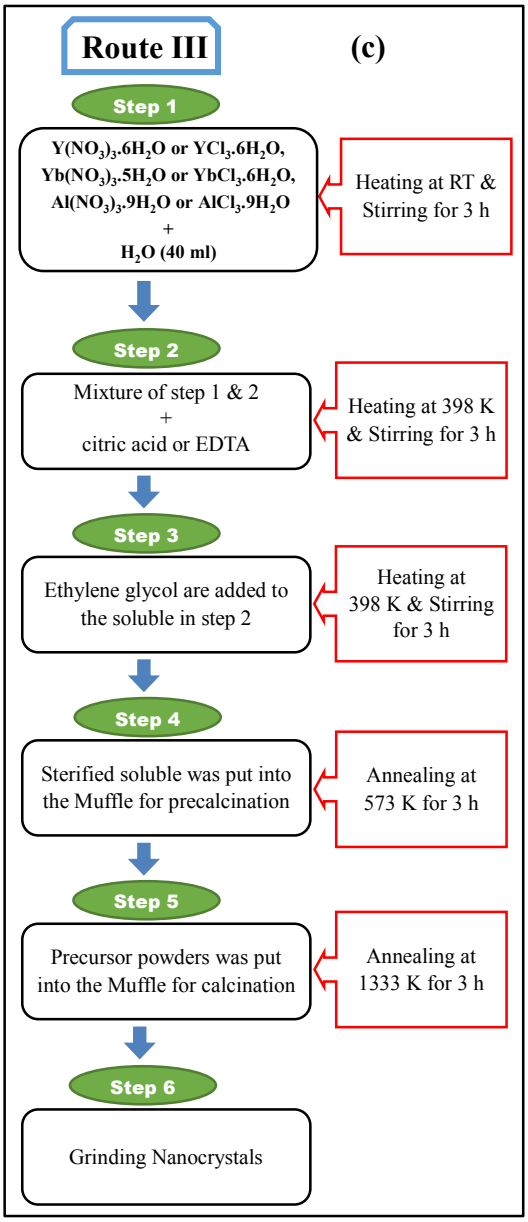

Figure 2.2. Flowchart of the modified Pechini method for Yb^{3+}-doped YAG nanocrystals synthesis in three different route. (c) Route III: The prepared nanoparticles from Exp. 21 to Exp. 40 were done by this type of synthesis.

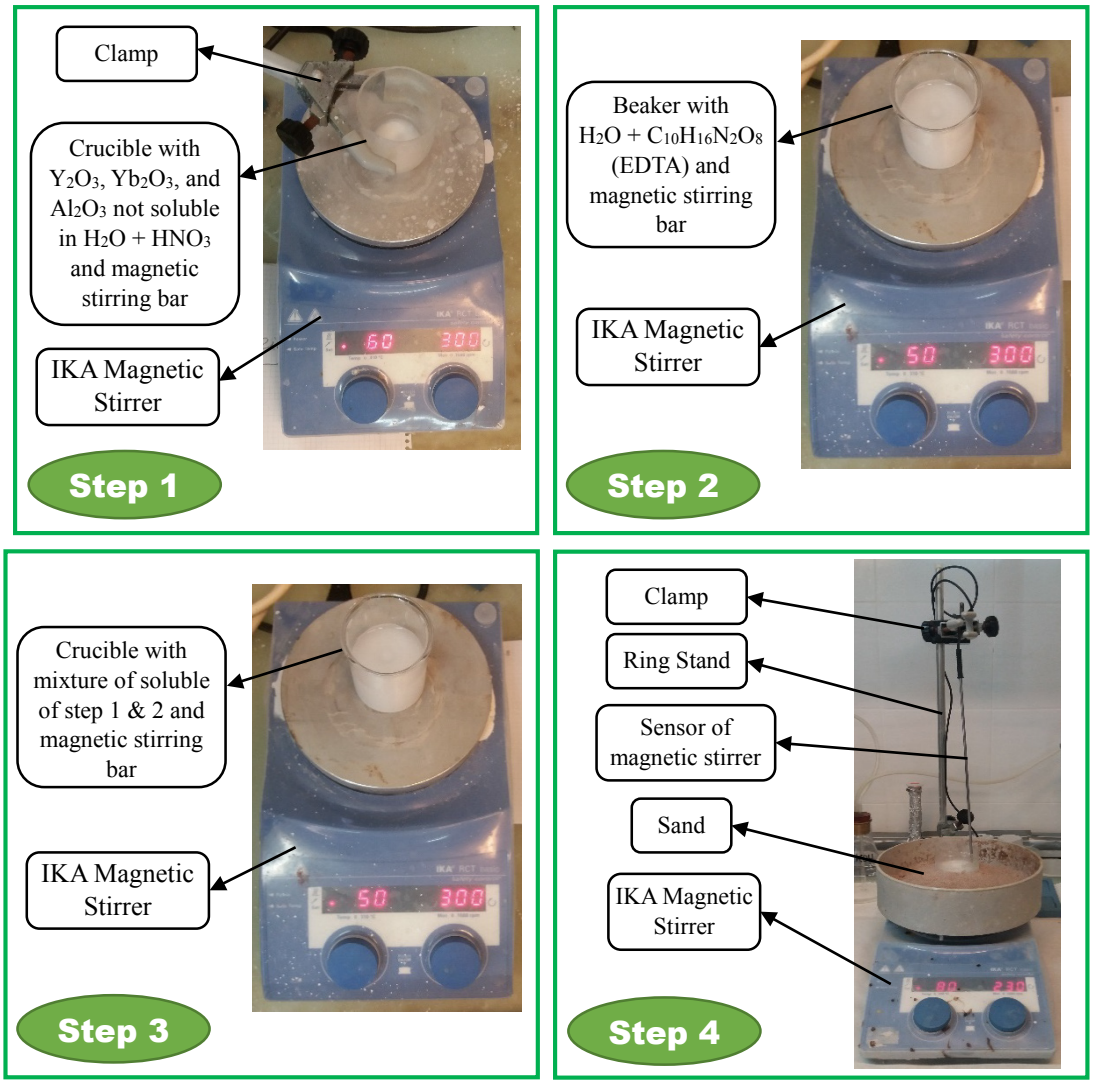

Figure 2.3. Experimental pictures of the Yb^{3+}:YAG nanocrystals preparation using the modified Pechini method from step 1 to step 4.

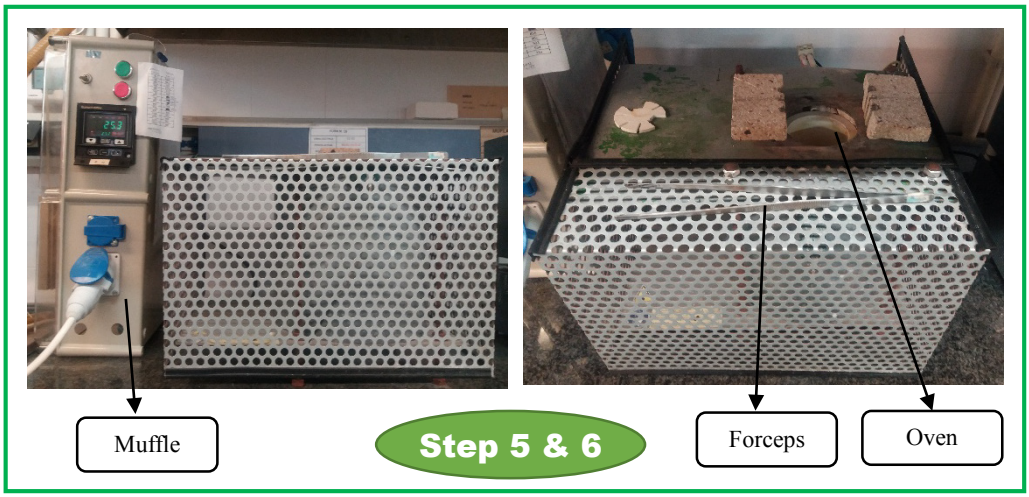

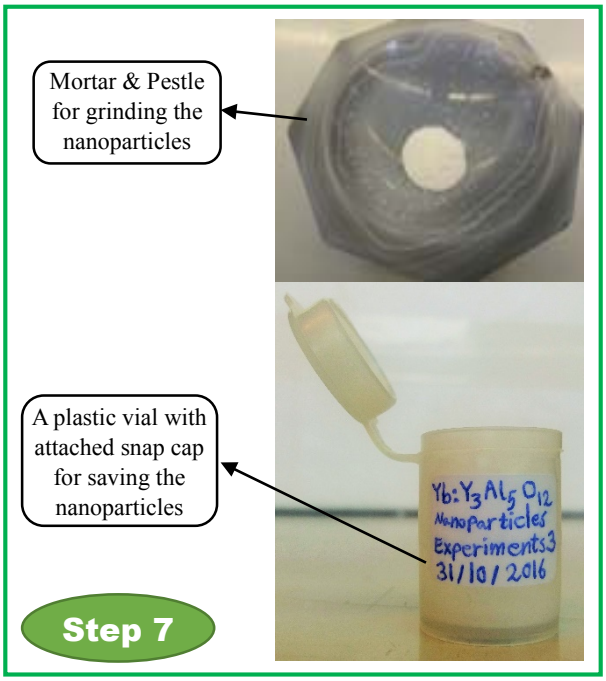

Figure 2.4. Experimental pictures of the Yb^{3+}:YAG nanocrystals preparation using the modified Pechini method from step 5 to step 7.

2.1.1. Route I

In brief, powders of Y_2O_3 (Aldrich, 99.99%), Yb_2O_3 (Alfa Aesar, 99%) or $Yb(NO_3)_3.5H_2O$ (Aldrich, 99.9%), and Al_2O_3 (Merck, γ-Tonerde) or $Al(NO_3)_3.9H_2O$ (Sigma-Aldrich, 98%) were utilized as beginning materials synthesize 5 at % Yb^{3+}:YAG nanoparticles. Stoichiometric amounts of yttrium oxide (99.9%), ytterbium oxide (99%) or ytterbium nitrate (99.9%), and were dissolved in HNO_3 (Labkem, 65%). For total evaporation of the liquid, the solution was sustained at 333 K.

Considering the complexing agent [CA] moles, the metal cations [METAL] moles, and the ethylene glycol [EG] moles, the following two molar ratios can be described;

$$C_M = \frac{[CA]}{[METAL]} \quad , \quad C_E = \frac{[CA]}{[EG]} \tag{3.1}$$

The microstructure of the produced particles is identified with these two proportions. The chelation procedure level of the metal in the natural production is defined by C_M. According to the low C_M ratios solutions (C< 1), it is possible to precipitate the metals salts on the solution and, consequently, nonuniformness in the chelation of the metals has occurred. The inadequate natural molecules to chelate metal cations is the expected reason. Two natural compositions, which were EDTA and citric acid, were applied as chelating agents. One metal ion is able to chelate with three bonds using one molecule of citric acid while it is capable of chelate with six bonds applying one molecule of EDTA. Therefore, the chelating power of EDTA to metal ions in compared with citric acid is more potent. Moreover, for moderately high C_M proportions, the dissolve of the metal ions is comfortable but the number of organics to be evacuated is ample [73]. Then, in this investigation Yb^{3+}:$Y_3Al_5O_{12}$ nanoparticles were synthesized without changing C_M ratio and it was used C_M = 1 and studied its effects.

The sterification degree of the chelating agent and the ethylene glycol is portrayed by C_E. It makes an unbending polyester network which diminishes each metals isolation in the procedure of the polymer disintegration at high temperatures [73]. The morphologies of the ceramic powder are influenced via the C_E ratio. The most porous is prompted via equimolar ratio [73]. The same as C_M, C_E=1 was used for our researching.

Simultaneously, powders of ethylenediaminetetraacetic acid, EDTA (Alfa Aesar, 99%) were solved within water at 323 K. The solutions were mixed together and the obtained solution was heated at 323 K for 3 h. The reaction of the esterification occurred once putting polyethyleneglycol (Aldrich, molecular weight 400) into the present solution. As a next step, to begin the decomposition of the organic resin, a pre-calcination at 603 K for 3 h was done. At last, the annealing of the precursor powder

was accomplished at 1277 K for 3 h at ambient atmosphere and afterward cooled down to RT. This route of the synthesis was done for Exp. 01, 02, 03, 04, 05, and 06 (see Figure 2.1a and Table 2.1.).

2.1.2. Route II

To sum up, powders of Y_2O_3 (Aldrich, 99.99%) or $Y(NO_3)_3.6H_2O$ (Alfa Aesar, 99.9%) or $YCl_3.6H_2O$ (Alfa Aesar, 99.9%), Yb_2O_3 (Alfa Aesar, 99%) or $Yb(NO_3)_3.5H_2O$ (Aldrich, 99.9%) or $YbCl_3.6H_2O$ (Alfa Aesar, 99.9%), and $Al(NO_3)_3.9H_2O$ (Sigma-Aldrich, 98%) or $AlCl_3.6H_2O$ (Aldrich, 98%) were used as starting materials to synthesize x at % Yb^{3+}:YAG nanoparticles, with x = 5, 10, 15, 30, 50. Stoichiometric amounts of yttrium oxide or yttrium nitrate or yttrium chloride (99.9%) and ytterbium oxide (99%) or ytterbium nitrate (99.9%) or ytterbium chloride (99.9%) were solved in HNO_3 (Labkem, 65%). In order to complete evaporation of the liquid, the solution was sustained at 423 K. Simultaneously, aluminium nitrate or aluminium chloride (98%) powders were solved within water at room temperature. The produced solution was blended with the nitrates manufactured and citric acid (Fluka, 99.5%) or EDTA (Alfa Aesar, 99%) and was kept for 3 h at 398 K. The reaction of the esterification happened once putting polyethyleneglycol (Aldrich, m.w. 400) into the available solution. As a next step, to begin the decomposition of the organic resin, a pre-calcination at 573 K for 3 h was done. At last, the annealing of the precursor powder was accomplished at 1333 K for 3 h at ambient atmosphere and afterward cooled down to RT. The prepared nanoparticles from Exp. 07 to Exp. 20 and from Exp. 41 to Exp. 48 were done by this route of synthesis (see Figure 2.1b, Table 2.1., and Table 2.2.).

2.1.3. Route III

In short, powders of $Y(NO_3)_3.6H_2O$ (Alfa Aesar, 99.9%) or $YCl_3.6H_2O$ (Alfa Aesar, 99.9%), $Yb(NO_3)_3.5H_2O$ (Aldrich, 99.9%) or $YbCl_3.6H_2O$ (Alfa Aesar, 99.9%), and $Al(NO_3)_3.9H_2O$ (Sigma-Aldrich, 98%) or $AlCl_3.6H_2O$ (Aldrich, 98%) were used as starting materials to synthesize x at % Yb^{3+}:YAG nanoparticles. Stoichiometric amounts of yttrium chloride (99.9%), ytterbium chloride (99.9%), and aluminum

chloride (98%) were dissolved in H_2O at RT. The obtained solution was mixed with citric acid (Fluka, 99.5%) and was kept for 3 h at 398 K. The reaction of the esterification happened once putting polyethyleneglycol (Aldrich, m.w. 400) into the existent solution. As a next step, to begin the decomposition of the organic resin, a pre-calcination at 573 K for 3 h was done. At last, the annealing of the precursor powder was accomplished at 1333 K for 3 h and afterward cooled down to RT. The prepared nanoparticles from Exp. 21 to Exp. 40 were done by this route of synthesis (see Figure 2.2. and Table 2.1.).

The synthesized Yb^{3+}:YAG nanoparticles through the three different routes of the Pechini method, which were explained in the above, were in various colors. Experimental picture of them has been taken by Samsung Galaxy J5 SM-J500F (White, 8GB). These colors were white and grey-white colors and in some cases yellowish, brown, and celadon colors (Colors given in Annex B).

Table 2.1. Summary of experiments for synthesizing the Yb^{3+}:YAG (In these experiments molar ratios C_M = [CA]/[METAL] and C_E = [CA]/[EG] were 1 and 2, respectively).

Experiment	Compound (at. %Yb at YAG)	Precursors			Complexing Agent		Pre-calcination temperature (K)	Calcination temperature (K)	Results
					EDTA (g)	Citric Acid (g)			
		Y_2O_3	Yb_2O_3	Al_2O_3					
1	5	0.5337	0.0431	0.4203	3.8657		603	1276	YAG + Y_2O_3 + $YAlO_3$ + $Y_4Al_2O_9$
2	5	0.5344	0.0430	0.4211	3.8670		603	1277	Mainly Re_2O_3 sesquioxides
2	5	0.5310	0.0429	0.4207	3.8660		603	1277	Mainly Re_2O_3 sesquioxides + other unidentified crystalline phase
2	5	0.5310	0.0429	0.4210	3.8662		603	1277	Mainly Re_2O_3 sesquioxides
3	10	0.4926	0.0845	0.4124	3.7877		603	1277	Mainly Re_2O_3 sesquioxides
4	15	0.4562	0.1233	0.4038	3.7120		603	1277	Mainly Re_2O_3 sesquioxides
5	20	0.4208	0.1618	0.3958	3.6386		603	1277	Mainly Re_2O_3 sesquioxides
		Y_2O_3	$Yb(NO_3)_3.5H_2O$	$Al(NO_3)_3.9H_2O$					
6	5	0.5311	0.1114	3.0948	3.8656		603	1277	Mainly Re_2O_3 sesquioxides + YAG
		Y_2O_3	Yb_2O_3	$Al(NO_3)_3.9H_2O$					
7	5	0.5313	0.0430	1.5478		2.5356	573	1277	Mostly YAM
7	5	0.5303	0.0435	1.5480		2.5351	573	1277	Mostly YAM
8	5	0.5303	0.0435	1.5480		2.5351	573	1333	Crystalline Solid (YAG + $Al_2Y_4O_9$)
9	5	0.5303	0.0435	1.5480		2.5351	573	1373	Crystalline Solid (less YAG + $Al_2Y_4O_9$)
		$Y(NO_3)_3.6H_2O$	$Yb(NO_3)_3.5H_2O$	$Al(NO_3)_3.9H_2O$					
10	5	1.8034	0.1161	3.0951		2.5350	573	1333	Crystalline Solid (YAG)
11	5	1.8016	0.1113	3.0940	3.8571		573	1333	Crystalline Solid (YAG + RE_2O_3)
11	5	1.8045	0.1117	3.0951	3.8580		573	1333	Crystalline Solid (YAG) The resulting nanocrystals were celadon.
		$YCl_3.6H_2O$	$YbCl_3.6H_2O$	$Al(NO_3)_3.9H_2O$					
12	5	1.4267	0.0990	3.0964		2.5371	573	1333	Crystalline Solid (YAG)
13	5	1.4294	0.0992	3.0949	3.8572		573	1333	Amorphous Solid
		$YCl_3.6H_2O$	$YbCl_3.6H_2O$	$AlCl_3.6H_2O$					
14	5	1.4279	0.0985	1.9939		2.5403	573	1333	Crystalline Solid (YAG) The resulting nanocrystals were celadon.

Table 2.1. (Contd.)

Experiment	Compound (at. %Yb at YAG)	Precursors			Complexing Agent		Pre-calcination temperature (K)	Calcination temperature (K)	Results
					EDTA (g)	Citric Acid (g)			
		$YCl_3.6H_2O$	$YbCl_3.6H_2O$	$AlCl_3.6H_2O$					
15	5	1.4293	0.0970	1.9975	3.8580		573	1333	Crystalline Solid (YAG) The resulting nanocrystals were celadon.
		$YCl_3.6H_2O$	$YbCl_3.6H_2O$	$AlCl_3.6H_2O$					
16	10	1.5391	0.1884	2.0338		2.5895	573	1333	Crystalline Solid (YAG) The resulting nanocrystals were celadon.
17	15	1.4276	0.2832	1.9943		2.5347	573	1333	Crystalline Solid (YAG) The resulting nanocrystals were celadon.
18	30	0.9528	0.5222	1.8039		2.2966	573	1333	Crystalline Solid (YAG) The resulting nanocrystals were celadon.
19	50	0.6324	0.8084	1.6790		2.1360	573	1333	Crystalline Solid (YAG) The resulting nanocrystals were celadon.
		$Y(NO_3)_3.6H_2O$	$Yb(NO_3)_3.5H_2O$	$Al(NO_3)_3.9H_2O$					
20	10	1.6734	0.2184	3.0319		2.4838	573	1333	Crystalline Solid (YAG)
21	15	1.5470	0.3204	2.9704		2.4360	573	1333	Crystalline Solid (YAG) The resulting nanocrystals were celadon.
22	30	1.2020	0.6047	2.8025		2.2975	573	1333	Crystalline Solid (YAG)
23	50	0.7989	0.9396	2.6060		2.1370	573	1333	Crystalline Solid (YAG)
		$YCl_3.6H_2O$	$YbCl_3.6H_2O$	$Al(NO_3)_3.9H_2O$					
24	10	1.3245	0.1889	3.0326		2.4838	573	1333	Crystalline Solid (YAG) The resulting nanocrystals were brownish.
25	15	1.2250	0.2765	2.9705		2.4355	573	1333	Crystalline Solid (YAG) The resulting nanocrystals were yellowish.
26	30	0.9518	0.5226	2.8022		2.2970	573	1333	Crystalline Solid (YAG) The resulting nanocrystals were yellowish.
27	50	0.6324	0.8075	2.6065		2.1356	573	1333	Crystalline Solid (YAG) The resulting nanocrystals were celadon.

Table 2.1. (Contd.)

Experiment	Compound (at. %Yb at YAG)	Precursors			Complexing Agent		Pre-calcination temperature (K)	Calcination temperature (K)	Results
		$Y(NO_3)_3.6H_2O$	$Yb(NO_3)_3.5H_2O$	$Al(NO_3)_3.9H_2O$	EDTA (g)	Citric Acid (g)			
28	10	1.6714	0.2208	3.0319	3.7787		573	1333	Crystalline Solid (YAG)
29	15	1.5460	0.3212	2.9710	3.7031		573	1333	Crystalline Solid (YAG + YAM + RE_2O_3)
30	15	1.5468	0.3221	2.9711	3.7034		573	1279	Crystalline Solid (YAG) The resulting nanocrystals were grey.
31	30	1.2019	0.6047	2.8033	3.4939		573	1333	Crystalline Solid (YAG)
32	50	0.7986	0.9393	2.6075	3.2483		573	1333	Crystalline Solid (YAG)
		$YCl_3.6H_2O$	$YbCl_3.6H_2O$	$AlCl_3.6H_2O$					
33	10	1.3244	0.1892	1.9526		2.4850	573	1333	Crystalline Solid (YAG)
34	15	1.2259	0.2769	1.9113		2.4353	573	1333	Crystalline Solid (YAG)
35	30	0.9543	0.5226	1.8041		2.2969	573	1279	Crystalline Solid (YAG) The resulting nanocrystals were grey.
36	50	0.6316	0.8071	1.6778		2.1360	573	1279	Crystalline Solid (YAG) The resulting nanocrystals were grey.
		$YCl_3.6H_2O$	$YbCl_3.6H_2O$	$AlCl_3.6H_2O$					
37	10	1.3230	0.1870	1.9520	3.7779		573	1279	Crystalline Solid (YAG)
38	15	1.2257	0.2791	1.9114	3.7018		573	1279	Crystalline Solid (YAG) The resulting nanocrystals were yellowish.
39	30	0.9536	0.5242	1.8044	3.4922		573	1279	Crystalline Solid (YAG) The resulting nanocrystals were grey.
40	50	0.6330	0.8079	1.6795	3.2476		573	1279	Crystalline Solid (YAG) The resulting nanocrystals were yellowish.

Table 2.2. Summary of experiments for synthesizing the undoped YAG (In these experiments molar ratios C_M = [CA]/[METAL] and C_E = [CA]/[EG] were 1 and 2, respectively).

Experiment	Compound	Precursors		Complexing Agent		Pre-calcination temperature (K)	Calcination temperature (K)	Results
		Y_2O_3	$Al(NO_3)_3.9H_2O$	EDTA (g)	Citric Acid (g)			
41	YAG	0.5710	3.160		2.5895	573	1173	Amorphous Solid
42	YAG	0.5710	3.160		2.5895	573	1277	Crystalline Solid (YAG dominant crystalline phase + $YAlO_3$ + $Y_4Al_2O_9$)
		$Y(NO_3)_3.6H_2O$	$Al(NO_3)_3.9H_2O$					
43	YAG	1.936	3.1592		2.5913	573	1333	Crystalline Solid (YAG)
44	YAG	1.9368	3.1618	3.9404		573	1333	Crystalline Solid (YAG)
		$YCl_3.6H_2O$	$Al(NO_3)_3.9H_2O$					
45	YAG	1.5351	3.1582		2.5901	573	1333	Crystalline Solid (YAG)
46	YAG	1.5338	3.1610	3.9413		573	1333	Amorphous Solid
		$YCl_3.6H_2O$	$AlCl_3.6H_2O$					
47	YAG	1.5331	2.1008		2.5929	573	1333	Crystalline Solid (YAG) The colors of synthesized nanocrystals were celadon.
48	YAG	1.5395	2.0432	3.9388		573	1333	Crystalline Solid (YAG) The colors of synthesized nanocrystals were celadon.

2.2. Structural And Microscopic Characterization Techniques

2.2.1. X-ray Diffraction (XRD)

X-ray crystallography or X-ray diffraction (XRD) depend on the disseminating of X-ray on a crystalline material, is an extremely helpful characterization instrument to perceive a crystal below the atomic and molecular structure, in which a beam of incident X-rays to diffract into numerous particular orientations are created via the crystalline atoms. A three-dimensional image of the density of electrons inside the crystal can be created by evaluating the angles and intensities of these diffracted beams and the atoms average locations within the crystal, chemical bonds of them, their disturbance and different other information can be specified through this electron density, as well [75].

Figure 2.5. illustrates a simple example of the reflection of X-rays by the atomic planes. After falling X-ray beam on the planes of atoms, several processes such as transmission, absorption, scattering, and diffraction may occur. However, constructive interference or reflection is obtained once the path of the wave scattered of the lower of the two planes is longer by an integer number of wavelengths λ than that of the wave scattered of the upper plane. It is established in the Bragg equation [76];

$$n\lambda = 2d_{hkl}\sin\theta \qquad (3.2)$$

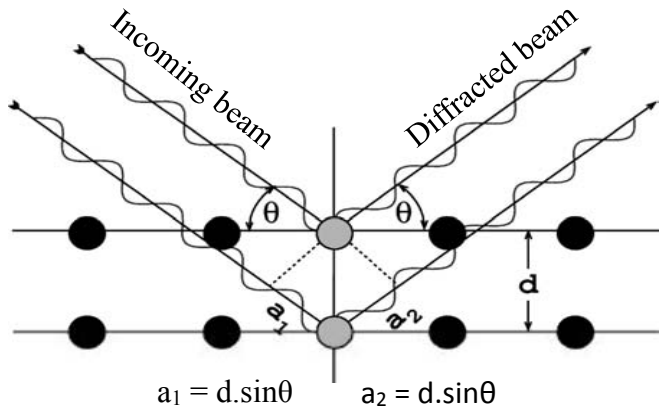

Figure 2.5. Scheme demonstrating the diffraction of X-rays by two sequential atomic planes [76].

Where (θ) is the angle between X-ray and the planes in the crystal, (λ) is wavelength of the incident X-ray beam, (d_{hkl}) is the spacing between the layers of atoms, (hkl) are Miller indices, and (n) is any integer representing the order of the diffraction peak. Therefore, we can easily calculate the distance between the atomic planes in a crystal by measuring the he angle of incidence of the X-ray beam.

Based on the nature of crystallite orientation required, two sorts of mounts for sample preparation for XRD is defined [77];

a. Random mounts are employed for distinguishing of phases in a sample. In this type of mount, particles ground to 1-5μm are collected to a flat surface onto a specimen holder to expect diverse orientations and guarantee reflections from different hkl planes [77].

b. Oriented mounts are utilized while investigating clay minerals which infrequently demonstrate strong diffraction impacts from Bragg planes other than the (00l). All in all, these are provided by construction a slurry of the specimen with distilled water. Then, the water is permitted to vaporize until the slurry is spread into a sample holder which could be a glass slide or ceramic tile [77].

So, in our case we utilized the random mounts for preparation our nanoparticles as we needed to identify of the Yb^{3+}:YAG nanocrystals phases. Then, the specimen through a range of 2θ angles were scanned, because of the accidental orientation of the powdered material, the whole lattice feasible diffraction directions were achieved. Due to a number of inimitable d-spacings of any crystal, the crystal recognition was possible through the conversion of the diffraction peaks to d-spacings. It is generally gained through the comparison of d-spacings with standard reference patterns by using the Joint Committee on Powder Diffraction Standards (JCPDS). It should be noted in 1978 the name of the organization was altered to the International Centre for Diffraction Data (ICDD) in order to highlight the global commitment of this scientific endeavor [78].

In this research, Yb^{3+}:YAG nanoparticles were characterized using two kind of X-ray diffractometer;

First, utilizing a Bruker-AXS D8-Discover diffractometer, the X-ray powder diffraction patterns were recorded. A Bruker-AXS D8-Discover diffractometer was accompanied by a parallel incident beam (Göbel mirror) and vertical theta-theta goniometer, XYZ motorized stage mounted on an Eulerian cradle, diffracted-beam Soller slits, a 0.2º receiving slit and a scintillation counter as a detector and the angular 2theta diffraction range was betwixt 5 and 70º. The gathering of data was done using an angular step of 0.05º at 3s per step. The acquisition of $Cu_{k\alpha}$ radiation was possible using a copper X-ray tube operated at 40 kV and 40 mA. The noted apparatus is accessible at the Servei de Recursos Científics i Tècnics of the Universitat Rovira i Virgili, Tarragona. A picture of this diffractometer is shown in Figure 2.6a.

Second, X-ray powder diffraction patterns were registered exploiting a Siemens D5000 diffractometer (Bragg-Brentano parafocusing geometry and vertical θ-θ goniometer) fitted with a curved graphite diffracted-beam monochromator, incident and diffracted-beam Soller slits, a 0.06º receiving slit and scintillation counter as a detector. The angular 2theta diffraction range was betwixt 4 and 40º. The cumulation of data was accomplished utilizing an angular step of 0.05º at 6s per step and specimen rotation. The attainment of $Cu_{k\alpha}$ radiation was conceivable applying a copper X-ray tube operated at 40 kV and 30 mA. The same as first equipment, this one is attainable at the Servei de Recursos Científics i Tècnics of the Universitat Rovira i Virgili in Tarragona, as well. A picture of this diffractometer is presented in Figure 2.6b.

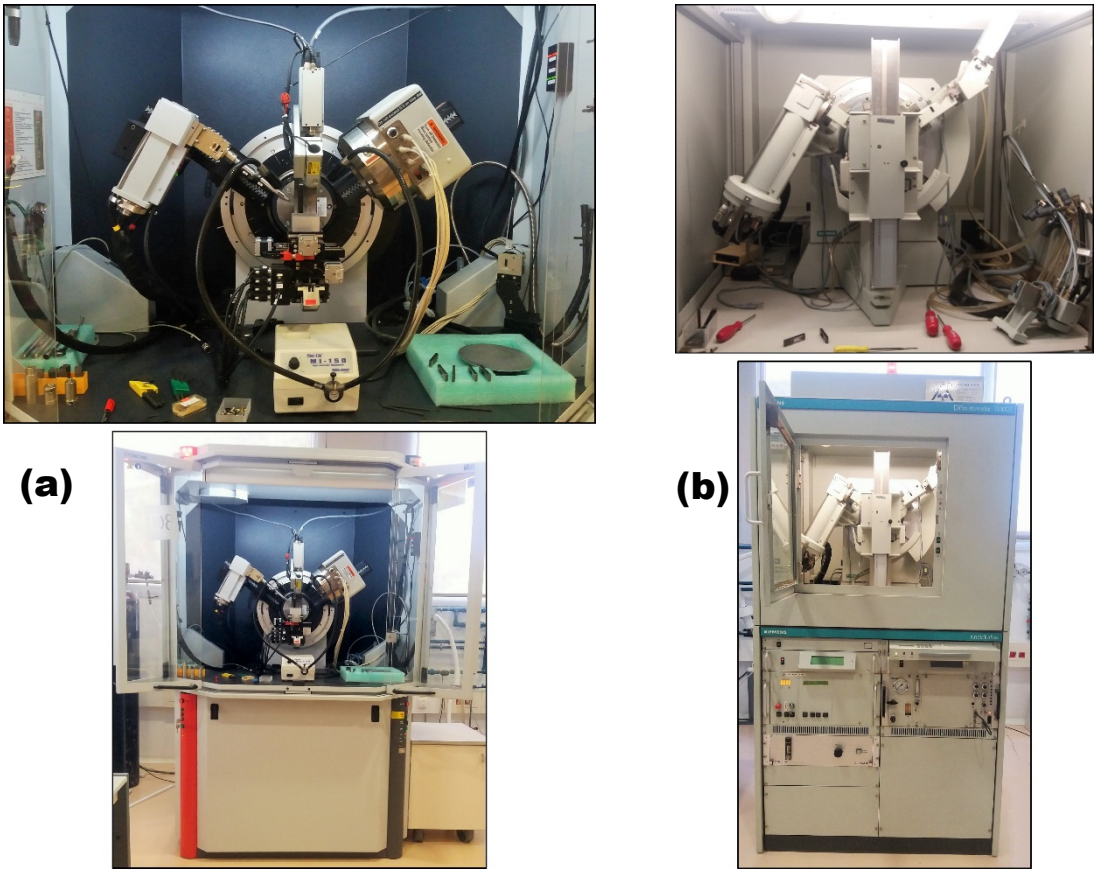

Figure 2.6. X-ray diffractometers' pictures which were used in this thesis. (a) Bruker-AXS D8-Discover diffractometer, (b) Siemens D-5000 diffractometer.

2.2.2. Transmission Electron Microscopy (TEM)

Transmission electron microscopy (TEM) was developed by Max Knoll and Ernst Ruska in 1931 in Germany as the primary electron microscope (EM) [79]. As a microscopy strategy, it utilizes a light of electrons with high energy to penetrate through a specimen to form an image. It can be noted that TEM uses various interaction of highly energetic electrons with the specimen: (i) unscattered electrons (transmitted beam); (ii) elastically scattered electrons (diffracted beam); (iii) and inelastically scattered electrons (absorbed beam). Diagram of this phenomena which is the resulting from the interaction of highly energetic electrons with matter is illustrated in Figure 2.7. After forming the image from the communication of the electrons with the sample, it is aggrandized and centralized onto a picturing apparatus, such as a fluorescent screen, a monitor, a layer of photographic film, or a sensor such as a charge-coupled device.

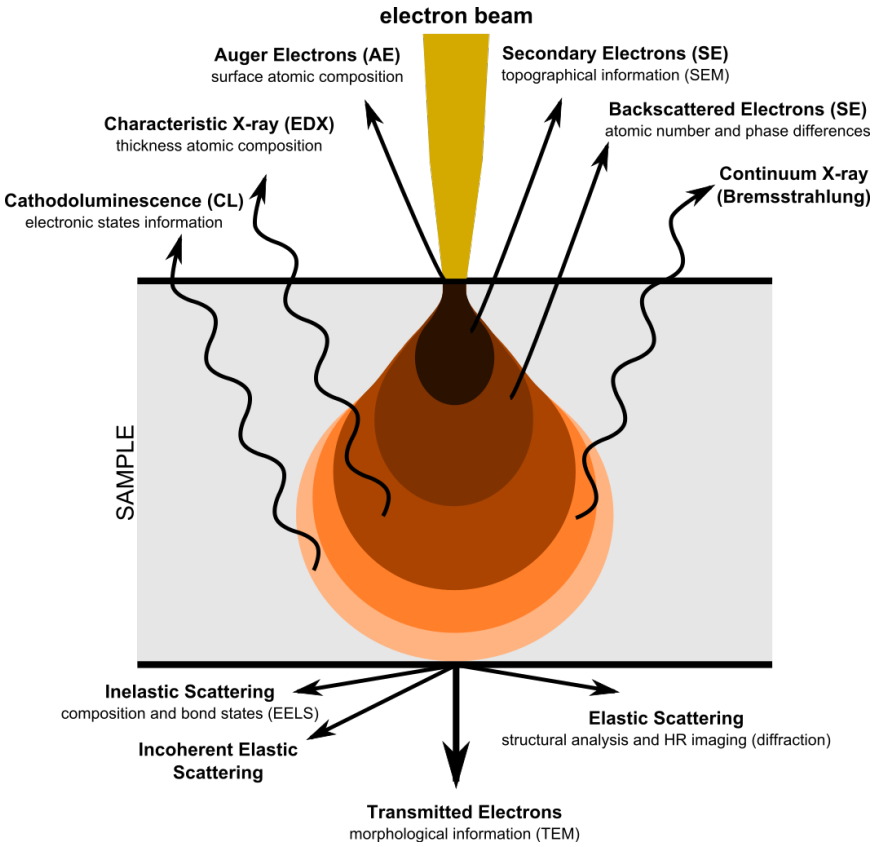

Figure 2.7. Diagram of the interaction of highly energetic electrons with the specimen [80].

In general, TEM system is comprised of three main components which are the illumination system, the objective lenses, and the imaging system. An electron source (tungsten filaments) and the condenser lenses for focusing are the two parts of the illumination system. Using the electron beam in a vacuum environment is obligatory due to the electrons are little and can be comfortably diverted via hydrocarbons or gas molecules available in the milieu. So, a set of pumps are exploited to perform enough vacuum in order to this aim in the column. For the sake of the creating a beam of electrons with the favorable diameter, the electron beam is expedited to an energy in the range 20-1000 keV, then the electron beam transmits using a number of condenser lenses. The objective lens and the sample holder, which is shown in Figure 2.8., is where all the beam-sample interactions happen. And at last, the imaging framework employed several lenses to magnify the image and to centralize them on the fluorescent screen or computer display utilizing a charge coupled detector (CCD) or a TV camera. A scheme of the TEM equipments used in this thesis is presented in Figure 2.9.

In this thesis, we utilized a JEOL JEM-1011 TEM apparatus, functioned at an accelerating voltage of 100 kV, outfitted with a CCD camera accessible at the Servei de Recursos Científics i Tècnics of Universitat Rovira i Virgili in Tarragona, to watch and describe the size distribution and morphology of the undoped YAG and Yb^{3+}:YAG nanocrystals (Figure 2.10.).

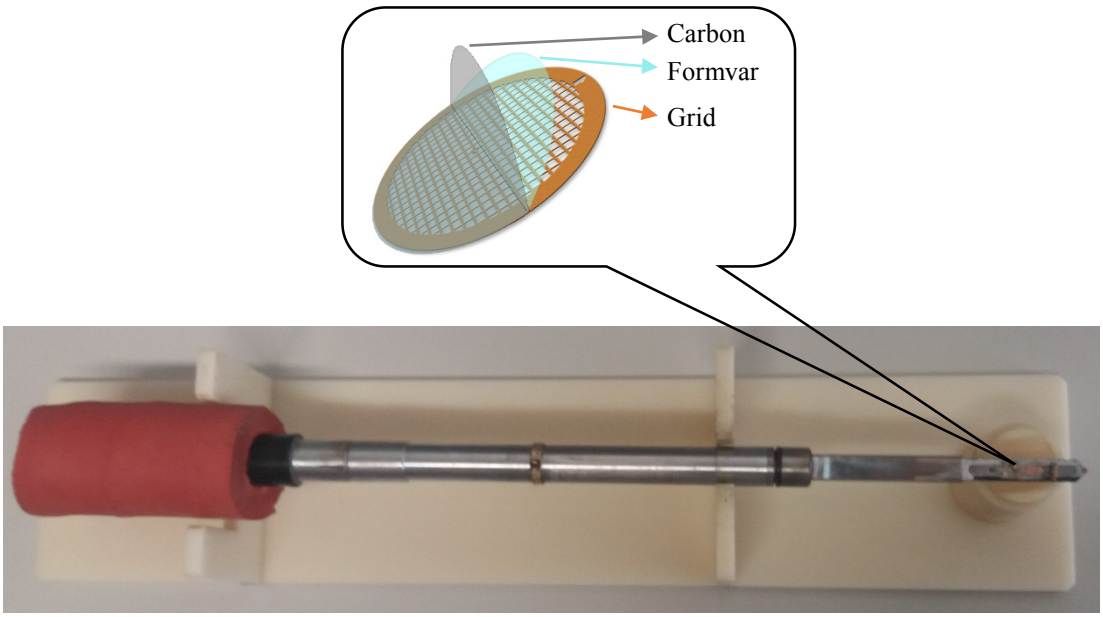

Figure 2.8. Picture of the sample holder with a mesh.

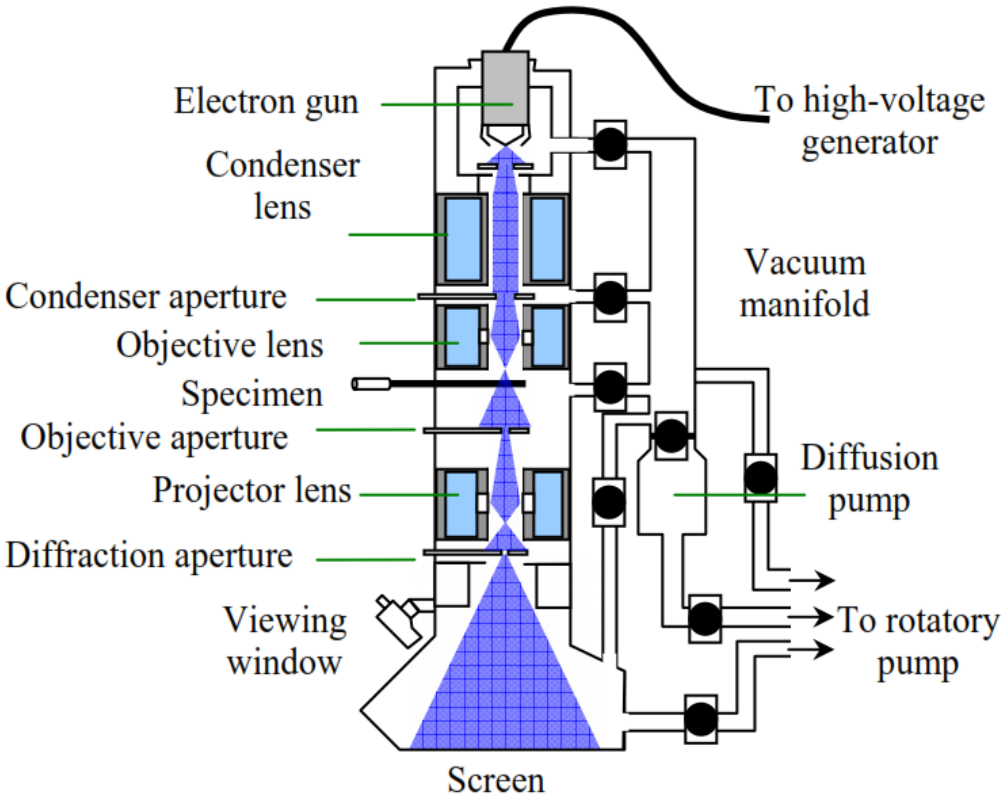

Figure 2.9. Schematic representation of the JEOL 1011 transmission electron microscope system used in the thesis.

Figure 2.10. Picture of transmission electron microscope JEOL JEM-1011.

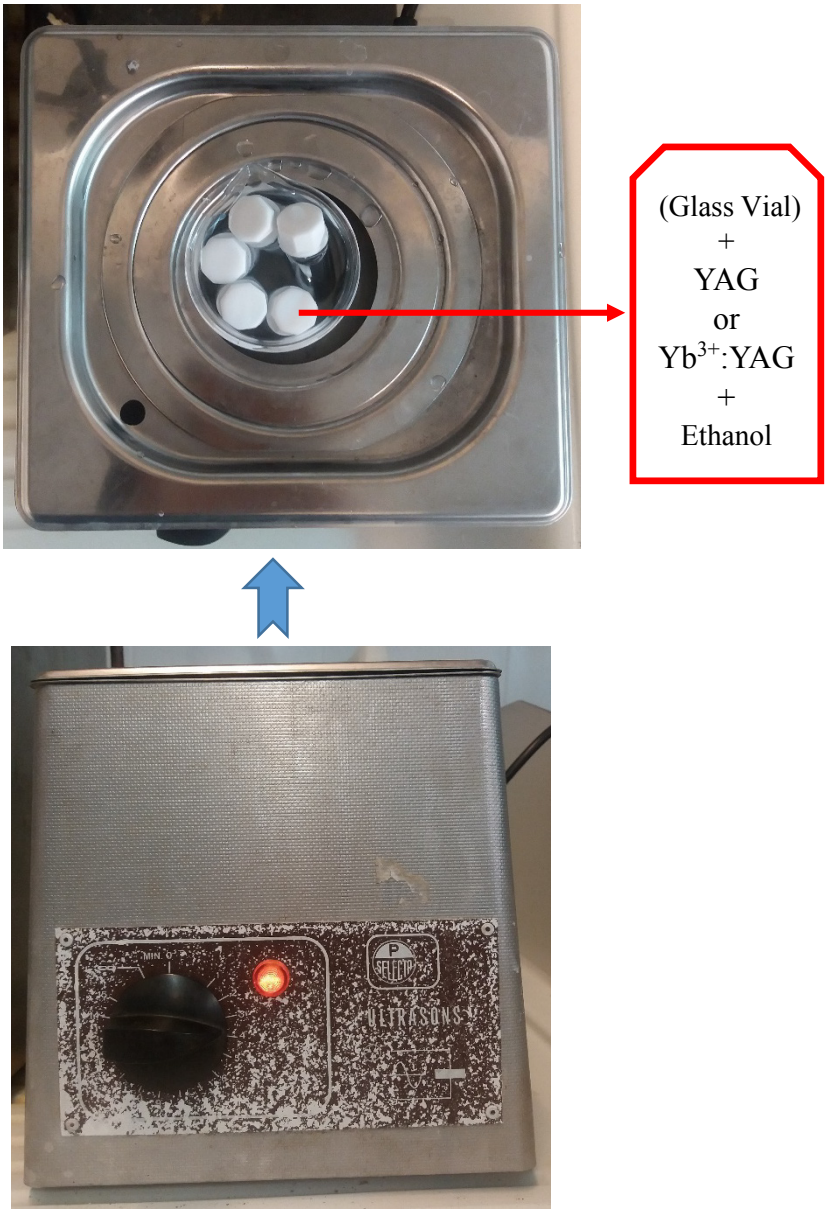

Figure 2.11. Picture of the Ultrasonic Cleaning Bath (P SELECTA, CD. 3000512).

For observation by TEM, it is necessary to prepare the synthesized nanoparticles which are the undoped YAG and Yb^{3+}:YAG. Therefore, 0.2 mg of nanocrystalline powder and 1 ml ethanol (Merck, pro analysis 99.8%) was putted in a glass vial and using the Ultrasonic Cleaning Bath (P SELECTA, CD. 3000512) was sonicated for 10 minutes (Figure 2.11.). Then, one drop of the resulting suspension was dropped on an amorphous carbon film (HD200 Fomvar/Carbon) supported on a 200 mesh copper grid (Figure 2.8.).

2.3. Spectroscopic Characterization Techniques

2.3.1. Photoluminescence Emission Measurements (PL)

By scanning the literature, it can be found different description for Luminescence. Emission of light by a matter which is not resulted from heat is called Luminescence [81]. In other words, it can be said that it is a form of cold-body radiation [81] or it can be considered as the inverse process of absorption, which means that it is the result of a spontaneous emission of photons after an electron relaxes from an excited or higher energy level to a lower energy level [82]. The electron can be excited by some form of energy (photons, electrons, heat, chemical reaction, etc.) [81]. Thus, there are many types of luminescence [81]. In the case of photons, it is called photoluminescence (PL) which is our interest of study. In general, it can be classified into two groups: fluorescence and phosphorescence. The emission lifetimes of the phosphorescence (> 10^{-3} s) is longer than fluorescence (> 10^{-8} s) [81].

Two kinds of setup were used in this thesis for photoluminescence emission measurements. These are the measurements of an absolute intensity and the measurements of fluorescence intensity ratio (FIR) which are explained in detail in the following subsections.

2.3.1.1. Measurements of an absolute intensity

To estimate the emission efficiencies of the samples, it is necessary to compare the absolute emission intensities of them. Thus, following the technique proposed by Boyer et al. [83] as shown in Figure 2.13., the measurements were done using an integrating sphere.

To describe the integrating sphere and its segments, it can be said that the generated light inside the integrating sphere is spreaded evenly by multiple reflections over the entire sphere surface. This is due to the fact that the sphere is made from a diffusive reflection material. Due to this reason, it is the ideal instrument for many applications

to compare the emission properties of the specimens such as laser power, optical flux, radiance, and reflectance measurements. There are three ports around the integrating sphere: detector, input, and output ports. Both of the input and output ports can be equipped with fiber adapters. There is a baffle inside the integrating sphere and besides the detector port to avoid the direct exposure to the incident light.

To determine the absolute intensity measurements, the Yb^{3+}:YAG NPs were placed in 1.5 mL borosilicate bottom flat vials (Figure 2.12.), slightly shaken to compact the powder, and placed inside an integrating sphere (Labsphere 4GPS-020-SL) (Figure 2.13b). Using a 980 nm InGaAs diode laser (Apollo Instrument, Inc. S50-980-2) connected to an optical fiber with a 20µm core diameter as the excitation light source (Figure 2.13a), and a collimator lens which centralizes the light onto the NPs inside a vial which were located into the integrating sphere. Finally, the generated signal by the NPs were gleaned using the fiber of a Yokogawa AQ6373 optical spectrum analyser (OSA) (Figure 2.13c). This setup is available at the FiCMA-FiCNA optical laboratory of the Universidad Rovira i Virgili, Tarragona. Scheme of this setup which is used to determine the spectra is shown in Figure 2.13.

Figure 2.12. Picture of a borosilicate bottom flat vials are used in this research.

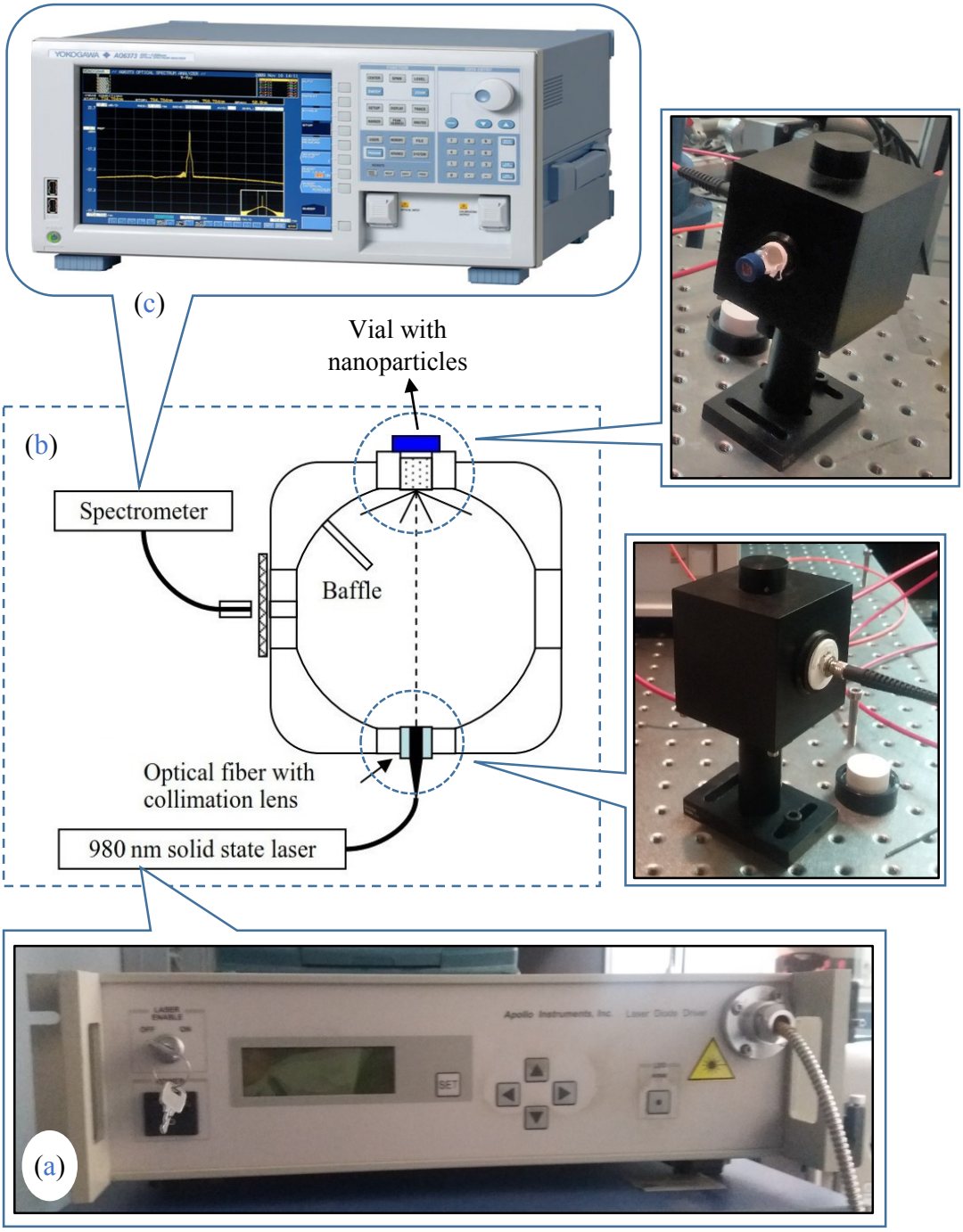

Figure 2.13. Scheme of the integrating sphere setup. (a) Picture of 980 nm InGaAs diode laser (Apollo Instrument, Inc. S50-980-2) connected to an optical fiber with a 20µm core diameter as the excitation light source, (b) Scheme of the Labsphere 4GPS-020-SL integrating sphere, Collimation lens, and the other optical components with their laboratory pictures, (c) Picture of a Yokogawa AQ6373 Series optical spectrum analyser (OSA).

2.3.1.2. Measurements of fluorescence intensity ratio (FIR)

As a goal of this research to develop a luminescent nanothermometer, it is necessary to study the temperature dependence of the luminescence properties of luminescent nanoparticles, ergo the fluorescence intensity ratio (FIR) technique is the best option.

For temperature dependent luminescence measurements, the Yb^{3+}:YAG NPs were placed in a Linkam THMS 600 heating stage to control the temperature of the samples. Then, they were excited with a diode laser (Monocrom, dual laser 810 nm / 940 nm) coupled to an optical fiber with emission at 940 nm (Figure 2.14a) or InGaAs diode laser (Apollo Instrument, Inc. S50-980-2) coupled to an optical fiber with a 20µm core diameter with emission at 980 nm (Figure 2.14b). The laser beam was paralleled by a collimation lens and was focused on the sample using a microscope objective (Olympus, 40X) (Figure 2.14d and Figure 2.15.). The NPs Near-infrared emission was collected by using the fiber of a Yokogawa AQ6373 optical spectrum analyser (OSA) (Figure 2.14c). This setup is available at the FiCMA-FiCNA optical laboratory of the Universidad Rovira i Virgili, Tarragona. The scheme of this setup and picture of the setup in the lab which is used to determine the spectra are shown in Figure 2.14. and Figure 2.15., respectively.

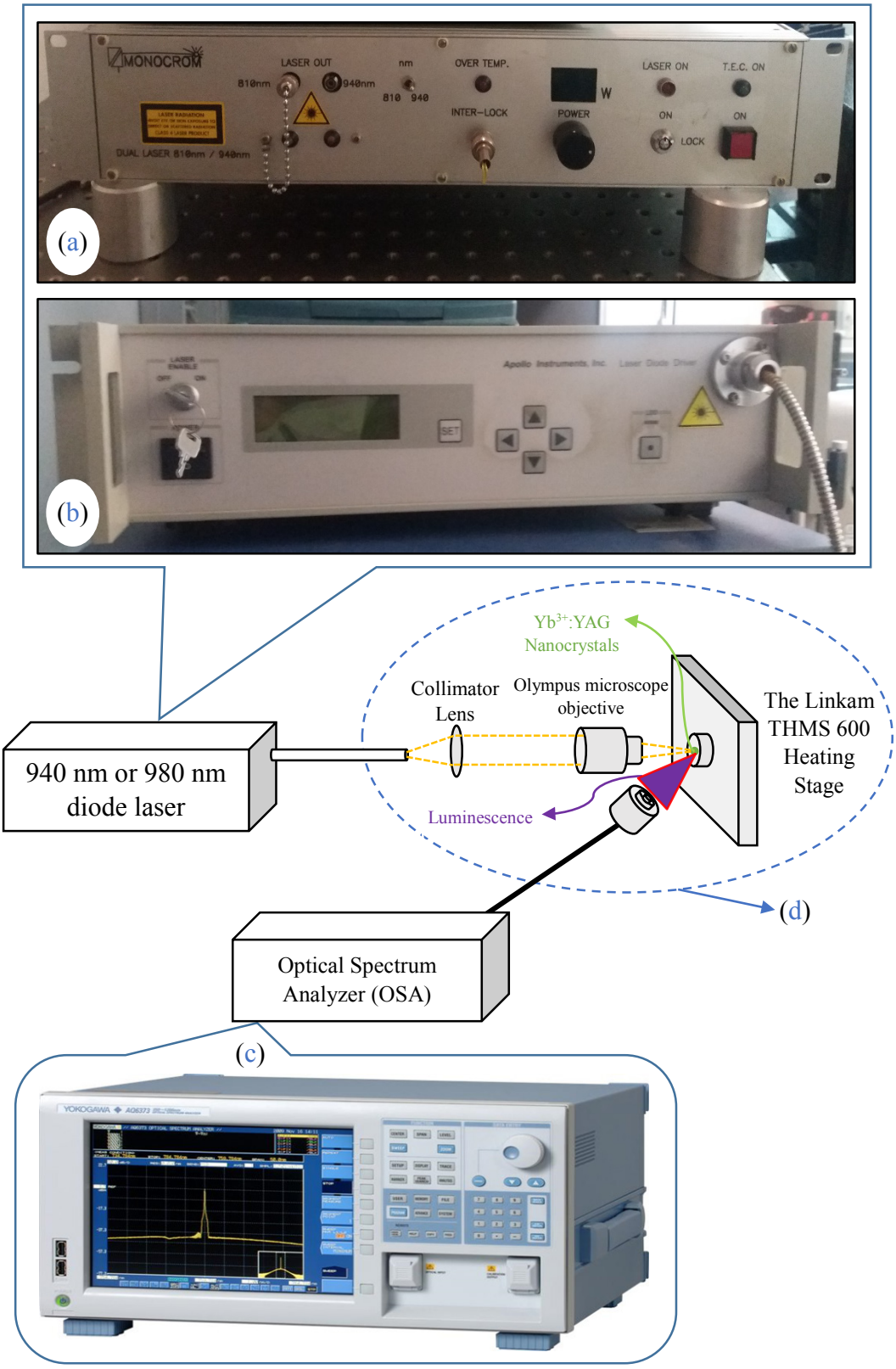

Figure 2.14. Scheme of fluorescence intensity ratio (FIR) setup. (a) picture of the fiber-coupled MONOCROM dual-wavelength diode laser, 808nm / 940nm, (b) Picture of 980 nm InGaAs diode laser (Apollo Instrument, Inc. S50-980-2) connected to an optical fiber with a 20µm core diameter as the excitation light source, (c) Picture of a Yokogawa AQ6373 Series optical spectrum analyser (OSA), (d) Scheme of the the Linkam THMS 600 heating stage, Olympus microscope objective, Collimation lens, and the other optical components.

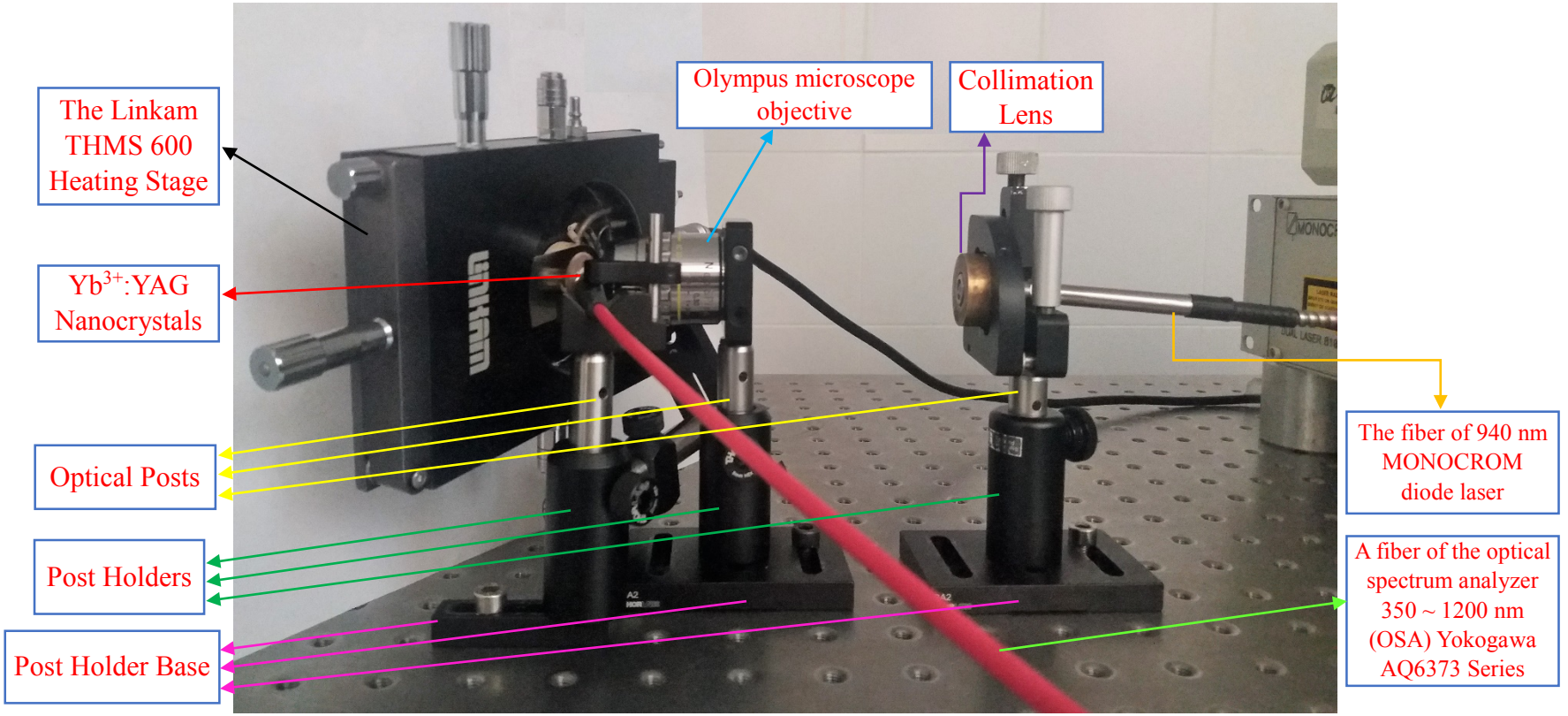

Figure 2.15. Picture of the Linkam THMS 600 heating stage, an Olympus microscope objective, Collimation lens, and the other optical components which were used in the FiCMA-FiCNA optical lab for measuring the fluorescence intensity ratio (FIR).

CHAPTER 3. EXPERIMENTAL RESULTS AND DISCUSSIONS

3.1. X-Ray Diffraction (XRD) Analysis

The obtained nanocrystals were constructionally portrayed using X-ray diffraction. Figure 3.1. and Figure 3.2. show the X-ray diffraction patterns of the Yb^{3+}:YAG and undoped YAG nanocrystals at different conditions for some selected experiments. By scanning and scrutinizing the XRD patterns of obtained products, the effect of the variables: - metal precursors, - the complexity agents, and - the calcination temperature which were applied for synthesis of nanocrystals has been studied.

3.1.1. Effect of the metal precursors

Effects of the metal precursors are discussed by using oxides, oxides with nitrates, nitrates, nitrates with chlorides, and chlorides. All of these effects are gleaned in the Table 3.1. and Table 3.2.

Using oxide precursors for all the metal cations of the YAG structure, XRD patterns of the obtained product does not match well with the JCPDs pattern corresponding to YAG (Figure 3.1i). It can be seen that mostly of the peaks indicate that the mainly the obtained product is the Re_2O_3 sesquioxides. It should be noted that in some cases we have got $YAlO_3$, $Y_4Al_2O_9$, and other unidentified crystalline compounds, as collected in Table 3.1. All by-products were in white color, as well.

It can be conluded that the products that their XRD patterns provided in Figure 3.1h and Figure 3.1i have similar characteristics and possess almost similar crystallinity degree, however, it seems that maybe one is more crystalline than the other.

By nitrates, XRD analysis depicted no extra peaks of residual or by-products (see Figure 3.2b, Figure 3.2c, and Figure 3.1f), since all the peaks observed in these patterns could be indexed confirming to the reference JCPDS 033-0040 pattern.

Applying either nitrates with chlorides or chlorides, the formation of YAG in the crystalline phase was confirmed by XRD analysis, as shown in Figure 3.1d, Figure 3.1b, and Figure 3.1a. The obtained patern in Figure 3.1b is in well aggreement with previously published paper [84]. The resulting product were in celadon, yellowish, and brown colour.

3.1.2. Influences of the complexity agents

To obtain the Yb^{3+}:YAG pattern, two natural compositions were utilized as chelating agents, CA, which were powders of citric acid and ethylenediaminetetraacetic acid, EDTA. We analyzed the effects of these materials using different metal precursors, which were explained in previous part. Table 3.1. and Table 3.2. show these effects with all details.

In both cases of using EDTA and citric acid, results did not show a significant difference once we used nitrates or chlorides as the metal precursors. In these conditions, YAG crystals were obtained (Figure 3.1a, Figure 3.1b which is well aggreement with previously published paper [84], Figure 3.1e, Figure 3.1f, Figure 3.2b, and Figure 3.2c). The only pattern changing was observed in Exp. 11. We obtain the YAG pattern by repeating that experiment.

In case of using nitrates with chlorides as precursors and EDTA as a complexity agent amorphous phases of nanoparticles was obtained (Figure 3.1c). Appling citric acid, per contra, crystalline solid was gained (Figure 3.1d).

3.1.3. Influences of the calcination temperature

To peruse the phase advancement, the precursor powders were calcined at several temperatures up to 1373 K. Crystalline phase investigation was then deciphered utilizing XRD.

In Figure 3.1i and Figure 3.1h, the X-Ray powder diffraction pattern of Yb^{3+}:YAG at 1277 K using oxides or oxides with nitrates as precursors and EDTA as chelating agent was not obtained.

At 1277 K using citric acid instead of EDTA with the same precursors, diffraction peaks of Yb^{3+}:YAG begin to show up and whatever remains of the peaks relate to YAM and YAP compounds, which are shown in Figure 3.1g and Figure 3.2a. By increasing the calcination temperature up to 1373 K in this circumstances, there was not observed considerable difference.

The formation of YAG in the crystalline phase, at 1333 K using nitrates or chlorides or both as precursors and EDTA or citric acid as chelating agents, was obtained. In case of using nitrates with chlorides and EDTA, the amorphous solid was obtained (Figure 3.1c).

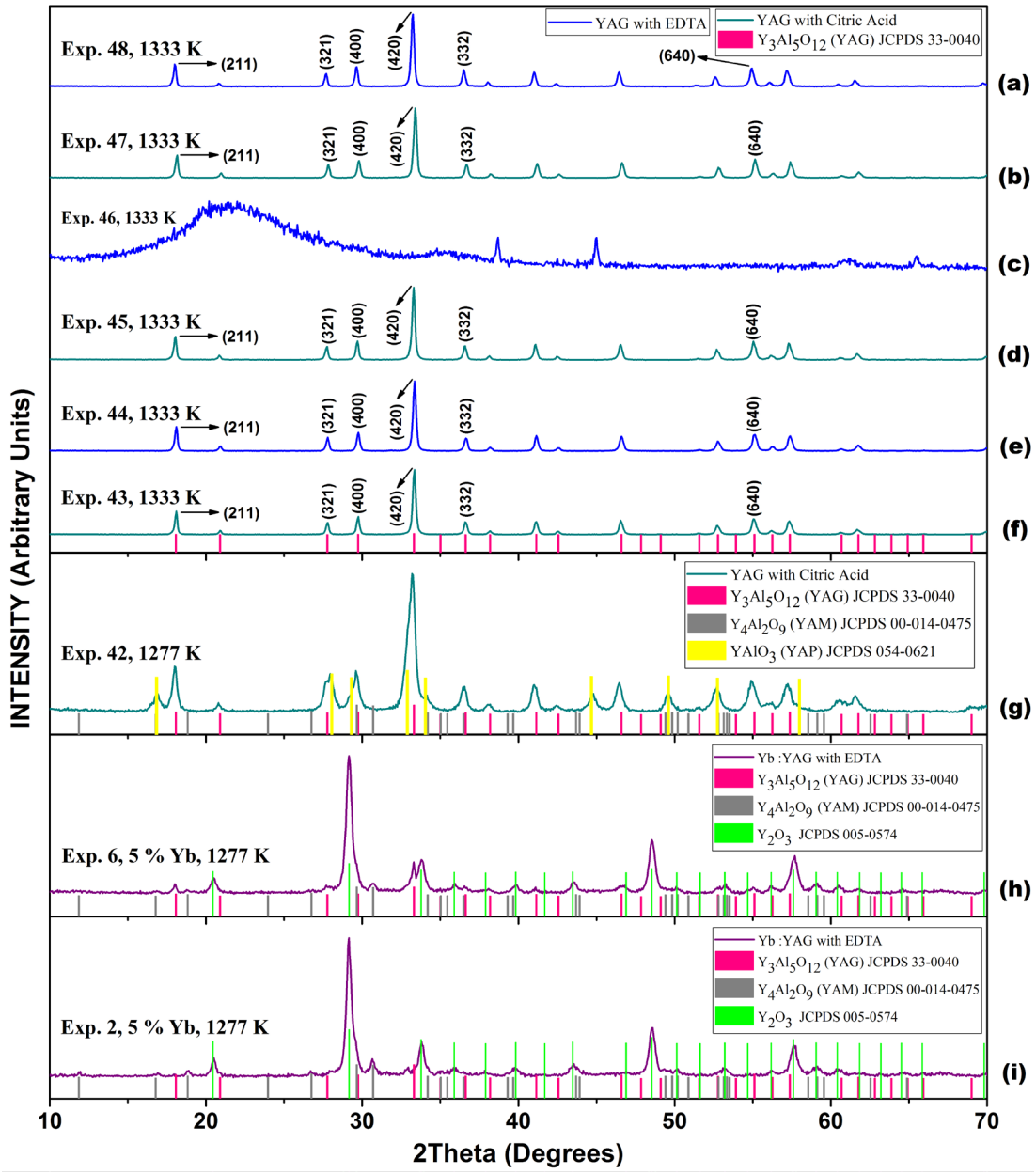

Figure 3.1. X-ray diffraction patterns of undoped YAG and Yb^{3+}:YAG nanocrystals obtained under different conditions. X-ray diffraction patterns of (a) undoped YAG with EDTA at a calcination temperature of 1333 K for 3 h using $YCl_3.6H_2O$ and $AlCl_3.6H_2O$ as precursors, (b) undoped YAG with citric acid at a calcination temperature of 1333 K for 3 h using $YCl_3.6H_2O$ and $AlCl_3.6H_2O$ as precursors, (c) undoped YAG with EDTA at a calcination temperature of 1333 K for 3 h using $YCl_3.6H_2O$ and $Al(NO_3)_3.9H_2O$ as precursors, (d) undoped YAG with citric acid at a calcination temperature of 1333 K for 3 h using $YCl_3.6H_2O$ and $Al(NO_3)_3.9H_2O$ as precursors, (e) undoped YAG with EDTA at a calcination temperature of 1333 K for 3 h using $Y(NO_3)_3.6H_2O$ and $Al(NO_3)_3.9H_2O$ as precursors, (f) undoped YAG with citric acid at a calcination temperature of 1333 K for 3 h using $Y(NO_3)_3.6H_2O$ and $Al(NO_3)_3.9H_2O$ as precursors, (g) undoped YAG with citric acid at a calcination temperature of 1277 K for 3 h using Y_2O_3 and $Al(NO_3)_3.9H_2O$ as precursors, (h) 5 at. %Yb at YAG with EDTA at a calcination temperature of 1277 K for 3 h using Y_2O_3, $Yb(NO_3)_3.5H_2O$, and $Al(NO_3)_3.9H_2O$ as precursors, (i) 5 at. %Yb at YAG with EDTA at a calcination temperature of 1277 K for 3 h using Y_2O_3, Yb_2O_3, and Al_2O_3 as precursors.

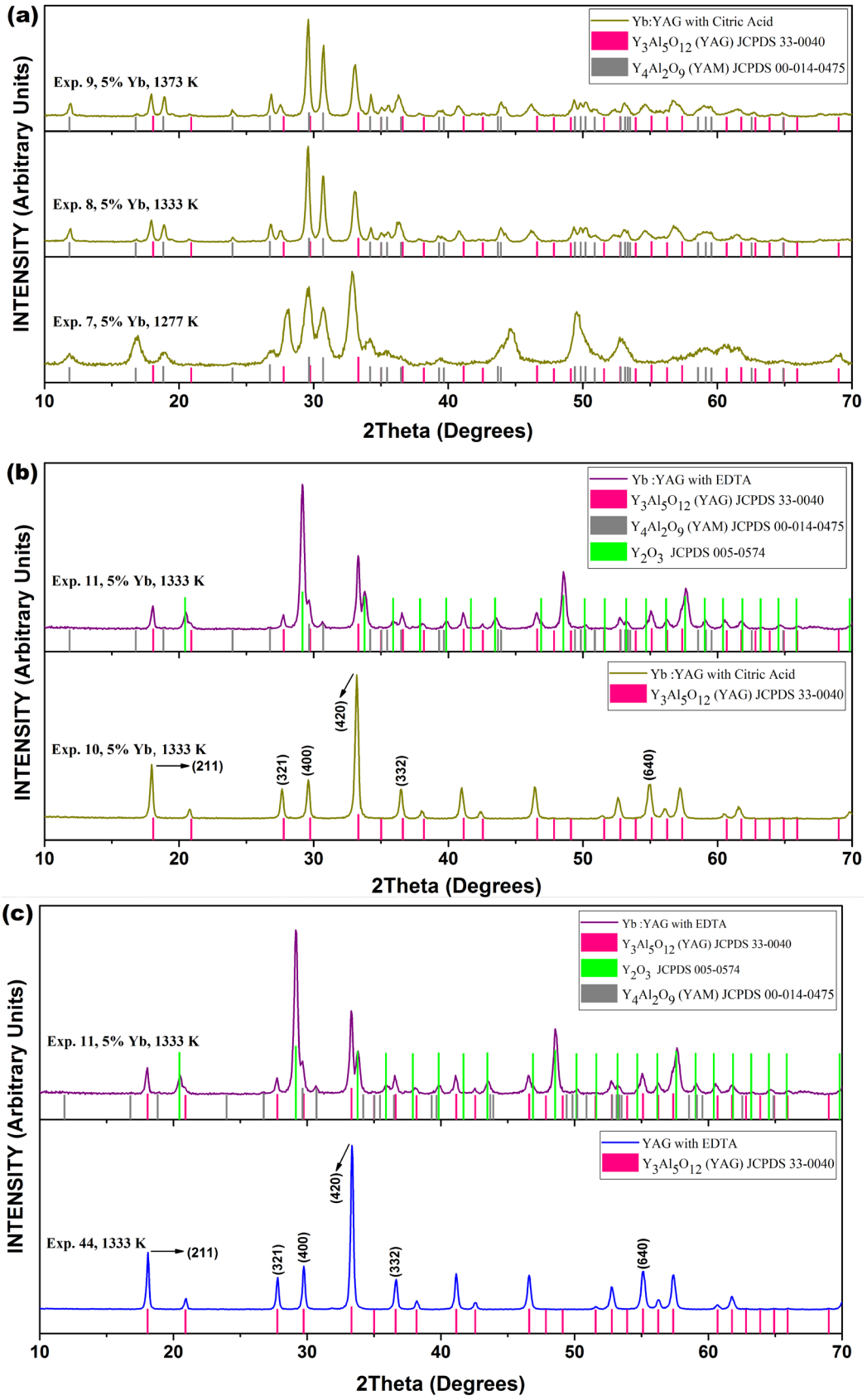

Figure 3.2. X-ray diffraction patterns of undoped YAG and Yb^{3+}:YAG nanocrystals obtained under different conditions.

The X-beam scattering datum and the Scherrer's formula [85] which connects the widening of the scattering peaks with the crystallite size [86], were utilized for deciding the crystallite size of the acquired nanocrystals;

$$L = \frac{0.9\lambda}{\beta.\cos\theta_B} \tag{4.1}$$

Where L is the crystallite size, β is the full width at half maximum (FHWM) [87] measured in radians on the 2θ scale, λ is the wavelength, and θ_B is the Bragg angle for the chosen hkl peak. The crystallite sizes were appraised utilizing the full width at half maximum (FWHM) of the (211), (321), (400), (420), (332), and (640) crests of the scattering pattern of undoped YAG nanocrystals, which are Exp. 43, 44, 45, 47, and 48, and 5 at% Yb^{3+}:YAG nanocrystals, which are Exp. 10 and 11. The calculated crystallite size of those experiments were summarized in Table 3.1.

3.2. Transmission Electron Microscopy (TEM) Analysis

Transmission electron microscopy (TEM) was applied to peruse the particle morphology, and size distribution. To examine the specimens by transmission electron microscopy (TEM), the nanocrystals were dissipated in ethanol (Merck, pro analysis 99.8%). Ultrasonication (P-SELECTA Ultrasons, CD. 3000512) was utilized to diminish and scatter the aggregates. Next, they were drop-thrown onto a copper grid secured by a permeable carbon film. The particle size distribution was evaluated utilizing TEM pictures, the Image J software, and OriginPro (64-bit) b9.3.226 software. Herein, TEM images of nanocrystals: - the undoped YAG and - the Yb^{3+}:YAG which were taken in different magnification have been analysed.

A size distribution of the particles must be situated in a solitary part of the size, and, in a perfect world, it must be identified with the usage. Once particles are round, the diameter is regarded ordinarily as the size perspective. Based on our situation, the nanocrystals lengths has been utilized because they are for the most part routinely formed. Nanoparticles shaped via nucleation, condensation, and particle development are anticipated to produce lognormal size distributions [88]. To obtain the information

for nanocrystals which are synthesized by the modified Pechini process, plotting particle size histograms were applied. Our nanocrystals size histograms are truly displayed via a lognormal distribution. To gain a unimodal nanosize distribution is the goal of this examination. In our case, the log distribution was fitted using the lognormal formula which is given by [88];

$$N(d) = A\left[\frac{-(\log d - \log d_0)^2}{2\sigma^2}\right] \tag{4.2}$$

Where N(d) is the number of particles with a determined length (d), A is the amplitude of the mode, d_0 is the mean of the studied parameter (length), and σ is the standard deviation of the mode (2σ is the dispersion of the mode). The fits were accomplished straightforwardly on the histogram information, and the outcomes are abridged in Figure 3.3., Figure 3.4., Figure 3.6., and Table 3.1.

3.2.1. TEM images of the undoped YAG

Figure 3.3. and Figure 3.4. depict TEM images of the two kinds of the undoped YAG nanocrystals: - without obtaining the YAG pattern which is the Exp. 42 and - with obtaining the YAG pattern which are the Exp. 43, 44, 45, 47, and 48.

In Figure 3.3a, pertaining to Exp. 42, the obtained nanoparticles have a spherical shape with irregular borders and non-defined crystalline grains. It can also be observed a large degree of agglomeration among the nanoparticles.

In Figure 3.3b, appertain to Exp. 43, the morphology of the nanocrystals is rather irregular but resembling an elongated sphere and non-defined crystalline grains. Sintering form of particles is obvious, as well. In accordance with the total size distribution histogram, the size of the nanocrystals is mainly in the range of 50-100 nm in length; the average size is 87.93 nm (in length).

In Figure 3.3c, which is related to Exp. 44, the spheroid nanoparticles are observed. There is no sintering form, and the range of the nanoparticles are 60-140 nm in length. In Figure 3.3d, corresponding to Exp. 45, the elongated sphere and sepheroid crystalline grains are observed. Sintering form of particles is found. By scanning the distribution histogram, the size of the nanocrystals is mainly in the range of 40-100 nm in length.

In Figure 3.4e, referring to Exp. 47, the ellipsoid or spheroid shape of the nanoparticles were seen. Sintering form of the nanoparticles is not found. Peeking in the distribution histogram, the size of the nanocrystals is mainly in the range of 40-120 nm in length.

In Figure 3.4f, referring to Exp. 48, the ellipsoid or spheroid shape of the nanoparticles were seen. Sintering form of the nanoparticles is not found. Peeking in the distribution histogram, the size of the nanocrystals is mainly in the range of 40-140 nm in length.

In conclusion, the nanoparticles which are synthesized using EDTA (see Figure 3.3c and Figure 3.4f) are bigger in comparison with those which are synthesized using citric acid (see Figure 3.3b, Figure 3.3d, and Figure 3.4e). Meanwhile, using the chlorides, more polyhedrical nanoparticles were obtained (Figure 3.4e, and Figure 3.4f). It should be noted that a large degree of agglomeration among the nanoparticles from TEM images of the experiments has been observed.

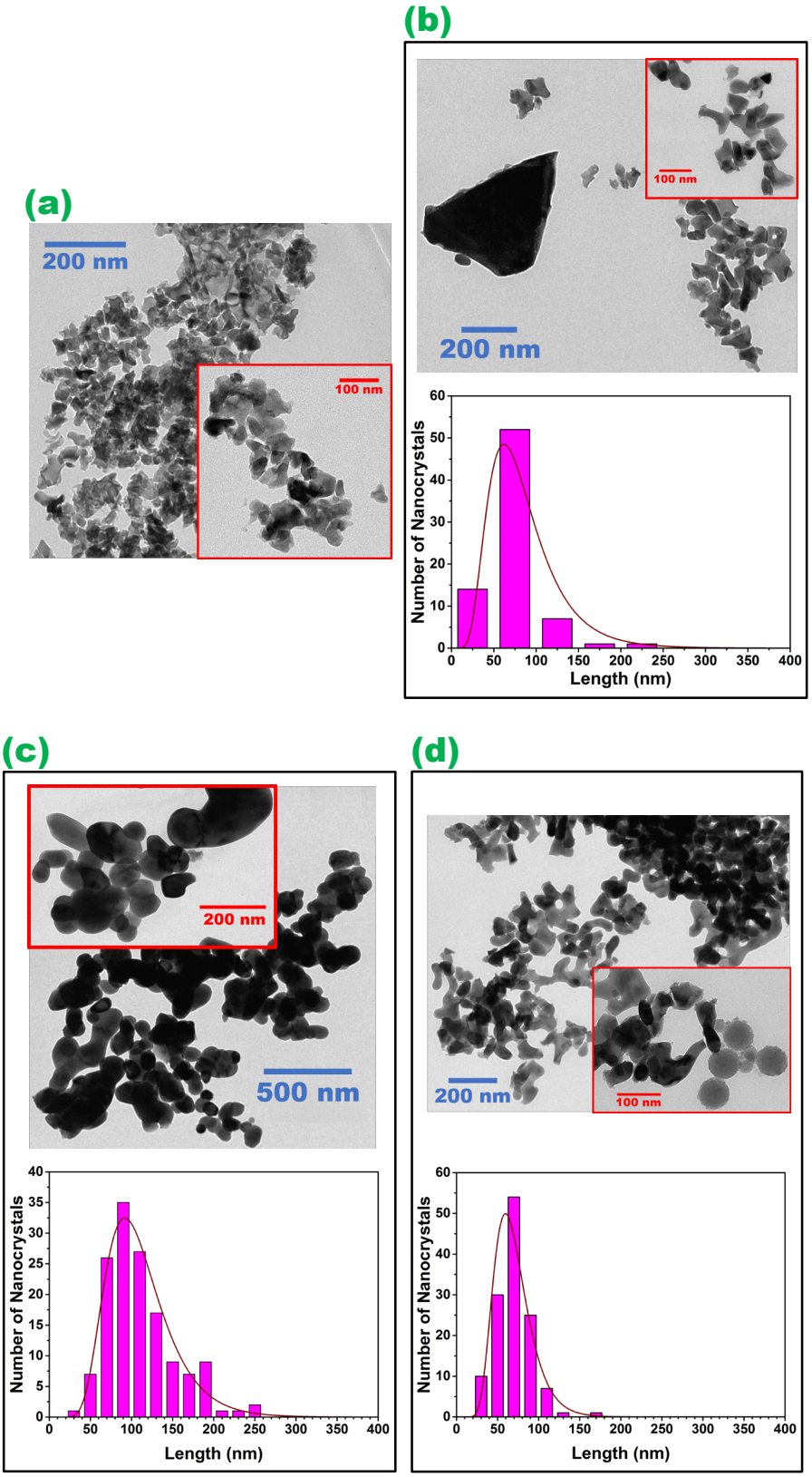

Figure 3.3. TEM photographs and size distribution histograms of the undoped YAG nanocrystals for (a) Exp. 42, (b) Exp. 43, (c) Exp. 44, (d) Exp. 45.

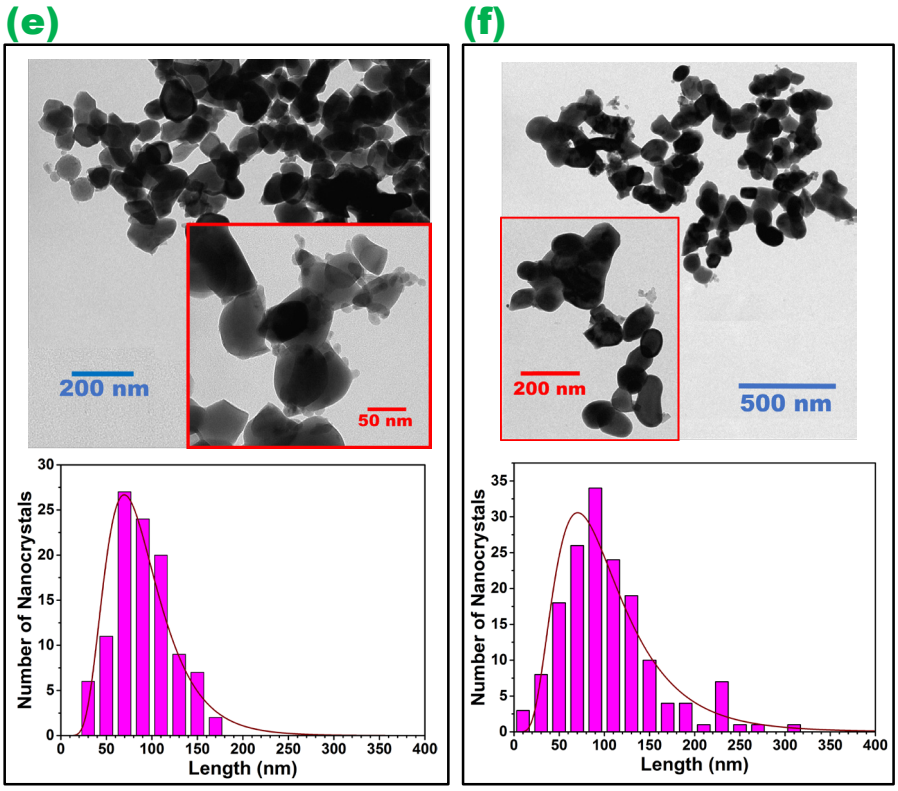

Figure 3.4. TEM photographs and size distribution histograms of the undoped YAG nanocrystals for (e) Exp. 47 and (f) Exp. 48.

3.2.2. TEM images of the Yb^{3+}:YAG

Akin to the undoped YAG nanocrystals, TEM images of the two kinds of the Yb^{3+}:YAG nanocrystals: - without obtaining the YAG pattern which are the Exp. 2, 6, 7, 8, and 9 and - with obtaining the YAG pattern which are the Exp. 10 and 11, are prepared. Figure 3.5. and Figure 3.6. show them.

In Figure 3.5a, corresponding to conditions of Exp. 2 in Table 3.1., the morphology of the nanocrystals is rather irregular but resembling a spheroid with irregular borders. The size of the nanocrystals is mainly in the range of 20-60 nm in length; the average size is 35 nm (in length). However, there are also unidentified nanoparticles.

In Figure 3.5b, which is related to Exp. 6, the elongated sphere and non-defined crystalline grains are observed.

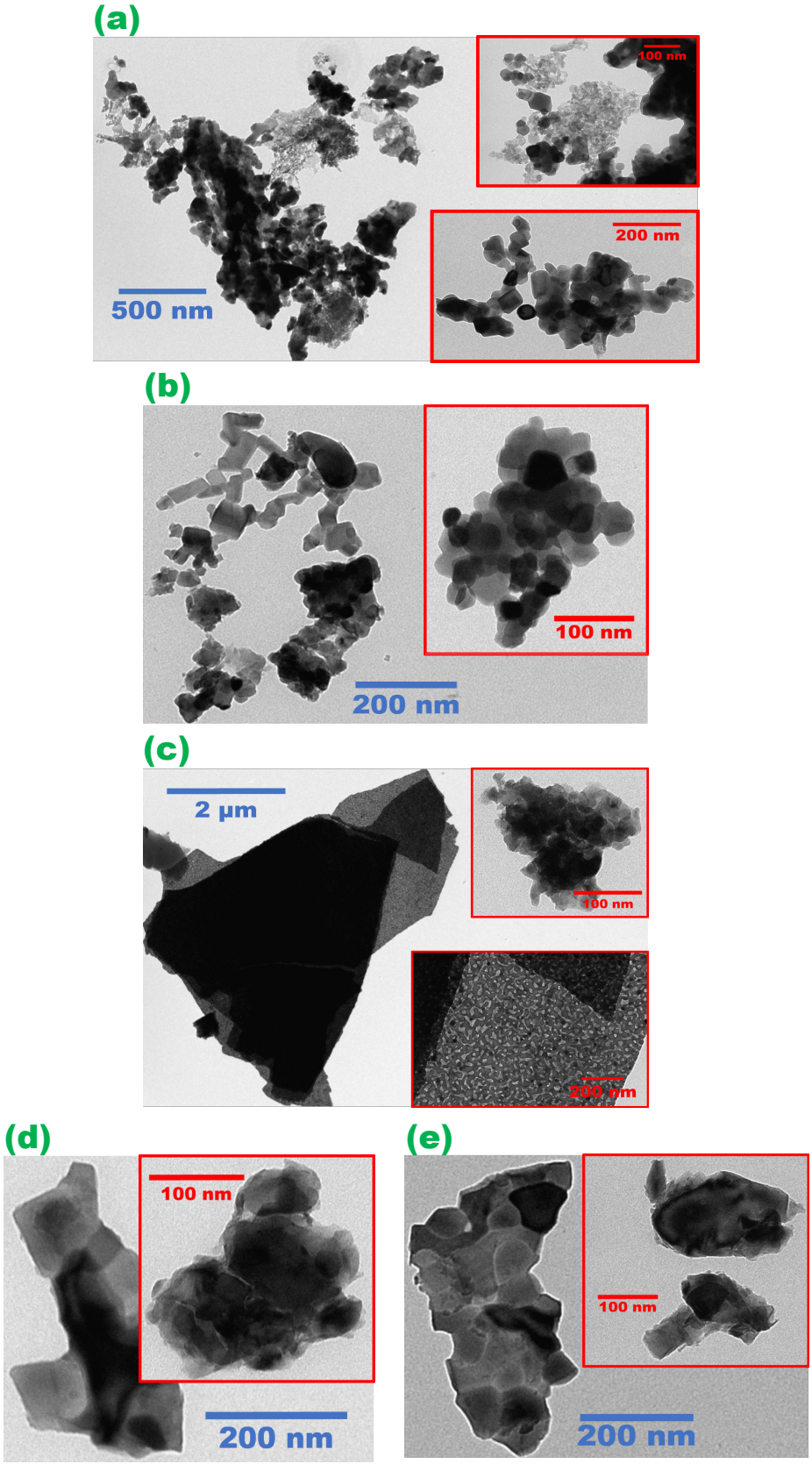

Figure 3.5. TEM photographs of Yb^{3+}-doped YAG nanocrstals for (a) Exp. 2, (b) Exp. 6, (c) Exp. 7 which was calcined at 1277, (d) Exp. 8 which was calcined at 1333, (e) Exp. 9 which was calcined at 1373.

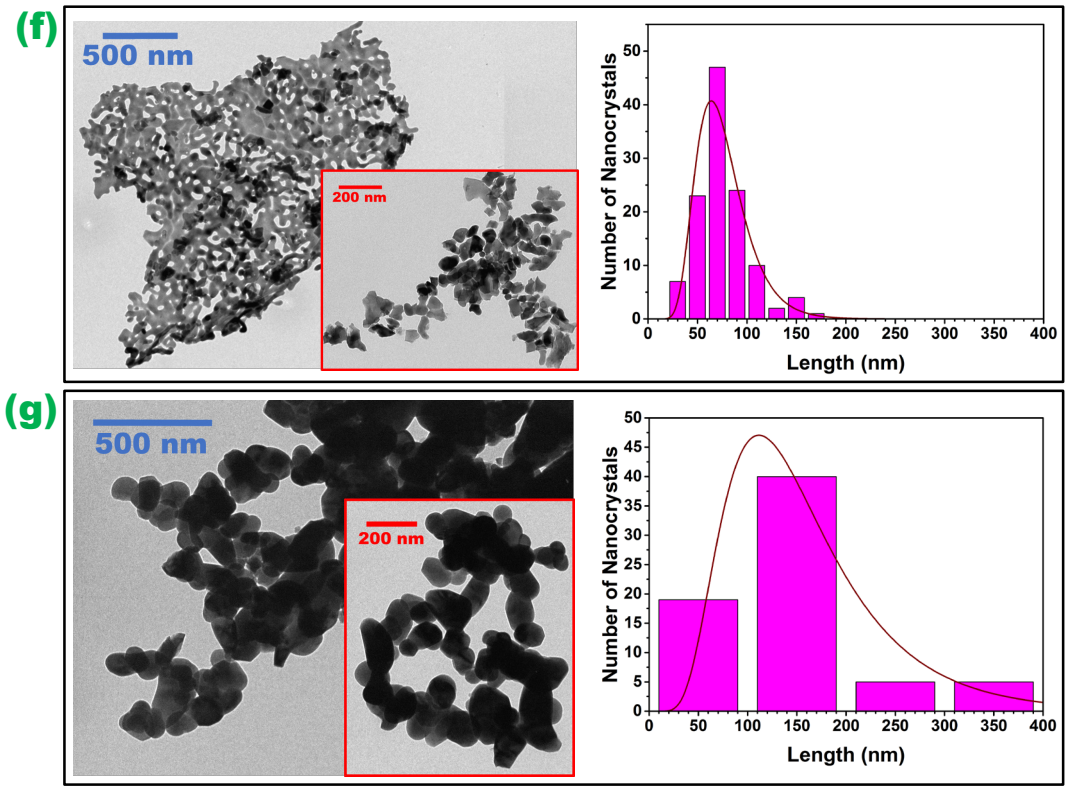

Figure 3.6. TEM photographs and size distribution histograms of Yb^{3+}:YAG nanocrstals for (f) Exp. 10 and (g) Exp. 11.

In Figure 3.5c, Figure 3.5d, and Figure 3.5e, connected to Exp. 7 at 1277 K, Exp. 8 at 1333 K, and Exp. 9 at 1373 K, non-defined crystalline grains are observed. It should be noted that a large degree of agglomeration among the nanoparticles from TEM images of these experiments has been observed. The YAG pattern of them, moreover, were not got as it mentioned in the XRD discussion.

In Figure 3.6f, appertain to Exp. 10, the crystalline kernels show the development of a repeated grid of the crystallites comprising of molded particles with rough fringes. The crystalline kernel measures evaluated of TEM pictures are mainly in the range of 40-100 nm in length. In addition, sintering form of the nanoparticles is more evident from images.

In Figure 3.6g, connected to Exp. 11, the establishment of a continued net of the crystallites comprising of kneaded particles with smooth faces were observed. The size of them is mainly in the range of 60-190 nm in length.

In conclusion, the nanoparticles which are synthesized using EDTA (see Figure 3.6f) are larger in comparison with those which are synthesized using citric acid (see Figure 3.6g). A large degree of agglomeration among the nanoparticles are seen simultaneously in TEM images.

Table 3.1. The undoped YAG and 5 at% Yb^{3+}:YAG nanocrystals sizes.

Undoped YAG		
Exp.	Crystallite size using the Scherrer's equation	Size of the nanocrystals using the distribution histogram
43	9.00 nm	50-100 nm
44	8.81 nm	60-140 nm
45	8.97 nm	40-100 nm
47	8.91 nm	40-120 nm
48	9.25 nm	40-140 nm
5 at% Yb^{3+}:YAG		
Exp.	Crystallite size using the Scherrer's equation	Size of the nanocrystals using the distribution histogram
10	7.98 nm	40-100 nm
11	8.43 nm	60-190 nm

3.3. Spectroscopic Characterization Of Yb^{3+}:YAG Nanocrystals

3.3.1. Absolute intensity analysis

To compare the absolute emission intensities of the samples in order to estimate their emission efficiencies the measurements were done using an integrating sphere (see Figure 2.13.).

Figure 3.7. shows the photoluminescence emission spectra of x at% Yb^{3+}:YAG nanocrystals, with x= 5, 10, 15, 30, and 50, at room temperature after excitation at NIR 980 nm collected in the integrating sphere. Every one of the specimens displays the main crest at 1030 nm, common of a crystalline Yb^{3+}-doped YAG matrix, as indicated by past works [89-93]. Some extra weaker peaks can likewise be seen close to this wavelength in some situations, because of the Stark splitting of the $^2F_{5/2}$ and $^2F_{7/2}$ spin-orbit multiplets of the Yb^{3+} ion. As can be seen in Figure 3.7., Exp. 10 shows the most intense emission among the whole experiments.

Thus, according to these results, nitrates with citric acid are the most efficient materials to generate emissions from Yb^{3+}:YAG nanocrystals in the near-infrared (NIR) region.

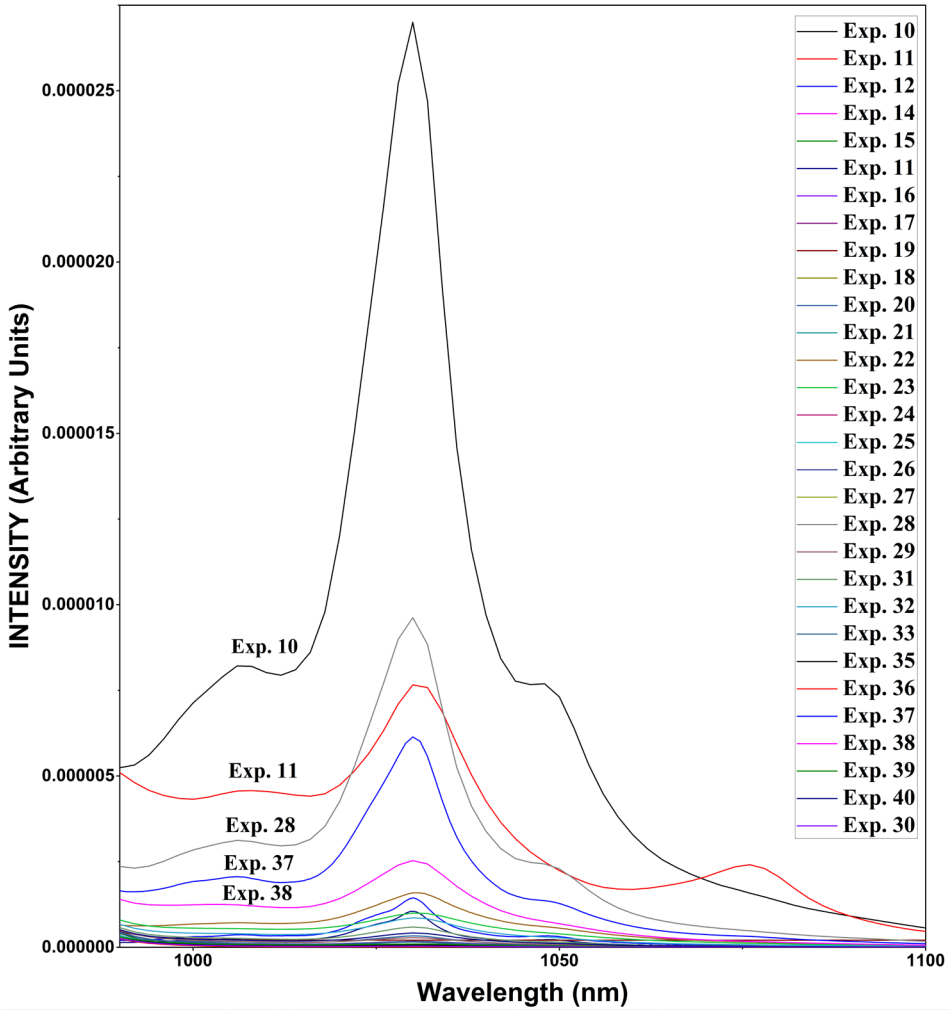

Figure 3.7. Absolute intensity of x at % Yb^{3+}:YAG nanoparticles, with x= 5, 10, 15, 30, and 50, at room temperature excited at 980 nm.

3.3.2. Fluorescence intensity ratio (FIR) analysis

In this work, we used Exp. 10 nanocrystals of Yb^{3+}:YAG as a proving of an idea of the practical assumptions of the thermometer using fluorescence intensity ratio (FIR) technique.

To appreciate the possible utilization of 5 at. % Yb^{3+}:YAG nanoparticles in order to thermic detecting, a satisfactory information of the thermic reaction of the intensity of the luminescence bands is a need. The emission spectra of these nanoparticles were

recorded using a diode laser (Monocrom, dual laser 810 nm / 940 nm) connected to an optical fiber after a pumping at 940 nm (see Figure 3.9a and Figure 3.9b) and the InGaAs diode laser (Apollo Instrument, Inc. S50-980-2) coupled to an optical fiber with a 20µm core diameter after a pumping at 980 nm (see Figure 3.10a, Figure 3.10b, and Figure 3.10c). Both of the emission specturms were obtained at room temperature (298 K), 303 K, 308 K, 313 K, 318 K, 323 K, 328 K, and 333 K, in the physiological area. The variation in the intensity of emission derived via temperature is seen in the four most strong crests, which are located at 1030 nm, 1048 nm, 1000 nm, and 1006 nm as if can be observed in detail in the Figure 3.9b and Figure 3.10c.

This enabled us to compute four various intensity ratios (thermal parameter) under excitation at 940 nm and 980 nm, correlating with the four emission bands achieved for Yb^{3+}, situating in the II-BW. Two different thermometric parameters were defined as the ratios for both of the excitations, first, the ratio betwixt the emission intensities of the $0' \rightarrow 2$ and $0' \rightarrow 3$ transitions corresponding to 1030 and 1048 nm peaks, second, the ratio betwixt the emission intensities of the $1' \rightarrow 3$ and $1' \rightarrow 2$ transitions referring to 1000 and 1006 nm peaks (see Figure 3.9b and Figure 3.10c). Accourding to the Figure 3.9c, Figure 3.9d, Figure 3.10d, and Figure 3.10e, the intensity proportions in any four states exhibited a relatively straight conduct in the intensity alteration in the biological scope of temperatures. Therefore, the theoretical parameter is given by the fitting of these experimental thermometric values in the following equations for each of the intensity rations;

$$\text{for 940 nm} \begin{cases} \Delta = 2.012 \times \exp\left(\frac{209.50}{T}\right) & (4.3) \\ \Delta = 0.72 \times \exp\left(\frac{-97.06}{T}\right) & (4.4) \end{cases}$$

$$\text{for 980 nm} \begin{cases} \Delta = 1.93 \times \exp\left(\frac{195.59}{T}\right) & (4.5) \\ \Delta = 0.82 \times \exp\left(\frac{-57.37}{T}\right) & (4.6) \end{cases}$$

Therein, the prognosticated calibration factors (the pre-exponential coefficients in Equations (4.3), (4.4) (4.5), and (4.6)) are 2.012, 0.72, 1.93, and 0.82, respectively. The thermometers performance can be deduced through the relative sensitivity, which is specified as the rate of variation of the FIR with temperature;

$$S_r = \frac{\Delta'}{\Delta} = \frac{1}{\Delta}\left|\frac{\partial \Delta}{\partial T}\right| \Rightarrow S_r = \frac{\Delta E}{kT^2} \times 100 \quad [\% K^{-1}] \tag{4.7}$$

The noted parameter has appeared in the physiologic scope in Figure 3.9e, Figure 3.9f, Figure 3.11f, and Figure 3.11g.

The values of the relative sensitivity under the excitation at 940 nm, between 0.236 – 0.188 % K^{-1} and 0.109 – 0.087 % K^{-1}, were observed (see Figure 3.9e and Figure 3.9f) while under the excitation at 980 nm, 0.220 – 0.176 % K^{-1} and 0.0646 – 0.0517 % K^{-1} values were seen (see Figure 3.11f and Figure 3.11g).

In order to better understand this process, according to the energy level diagram, the thermometer designing has displayed in Figure 3.8.

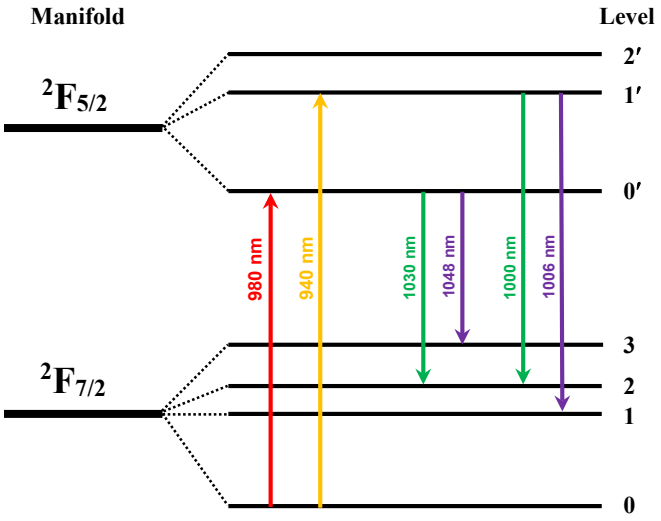

Figure 3.8. A schematic energy level diagram which is utilized to resembling the energy levels of the Yb^{3+} ion engaged with the thermometer performance.

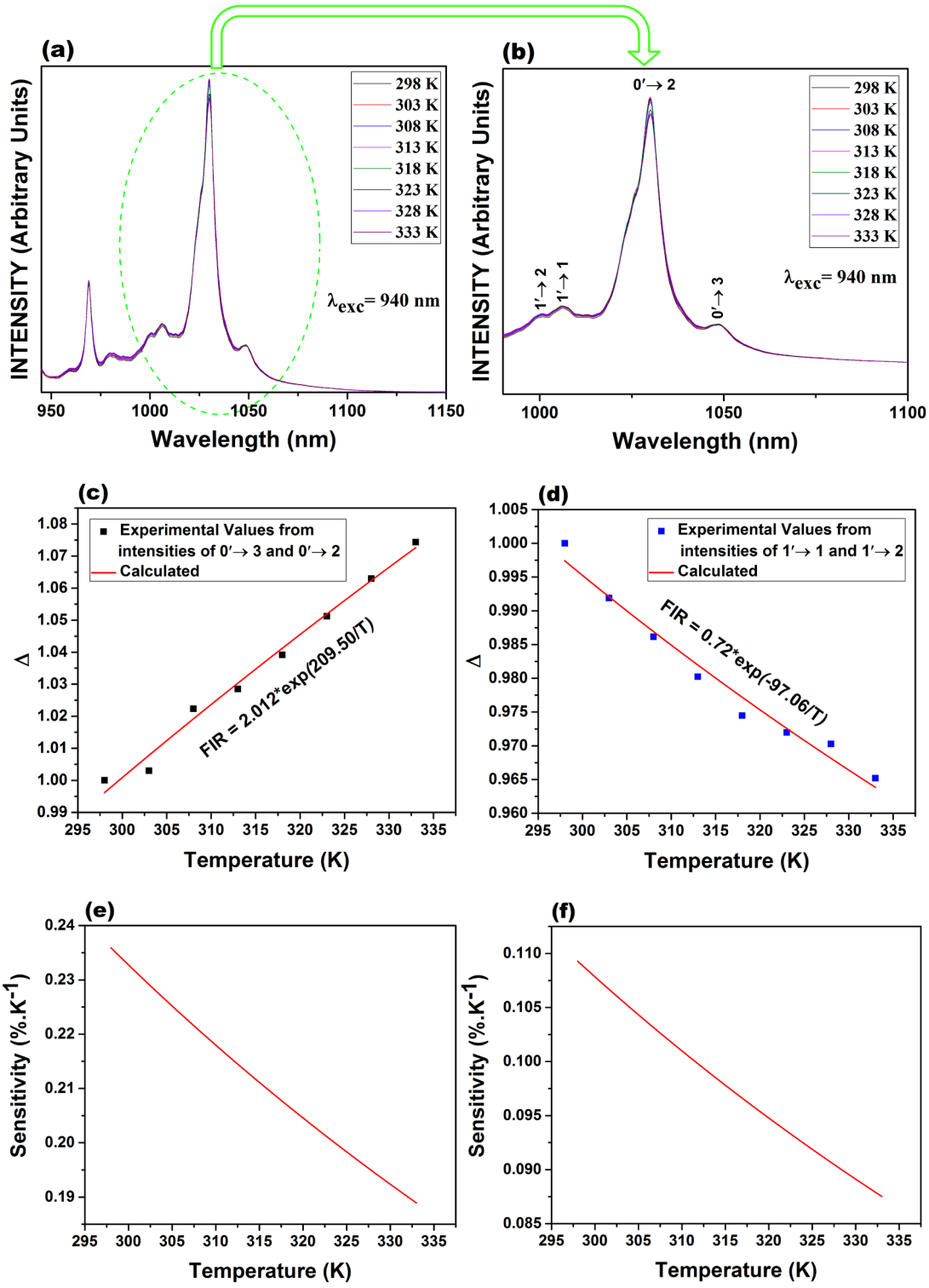

Figure 3.9. (a) Emission spectra of Yb^{3+}:YAG nanoparticles after pumping at 940 nm in the 945-1150 nm region. (b) Emission spectra of Yb^{3+}:YAG nanoparticles after pumping at 940 nm in the 900-1150 nm region. (c), (d) Thermometric parameters for the physiologic scope. Dots are the experimental amounts from the Δ parameter gained of the spectra in (a). (e) Relative sensitivity of (c) in the physiologic scope. (f) Relative sensitivity of (d) in the physiologic scope.

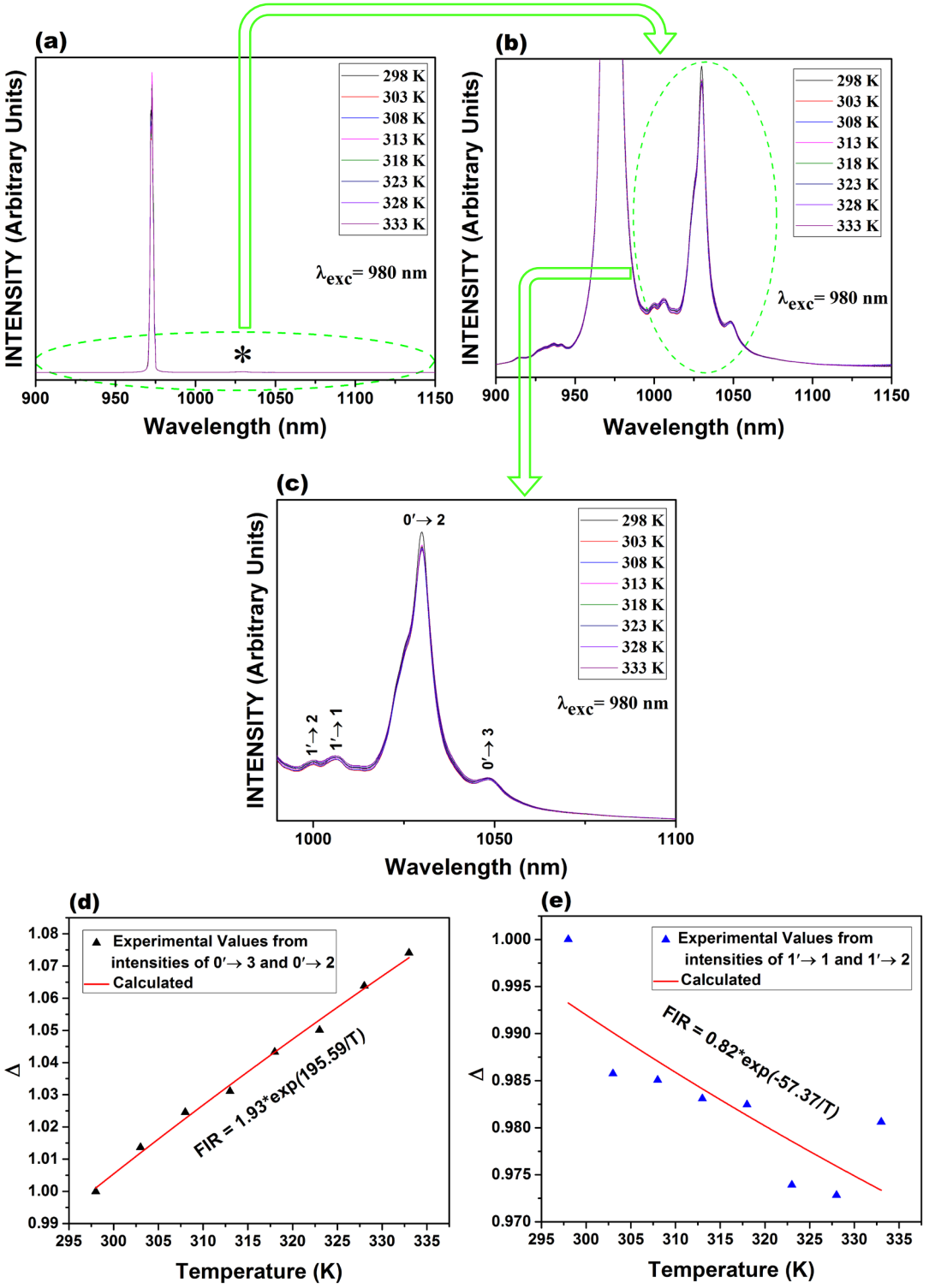

Figure 3.10. (a), (b) Emission spectra of Yb^{3+}-doped YAG nanoparticles after pumping at 980 nm in the 945-1150 nm region. (c) Emission spectra of Yb^{3+}:YAG nanoparticles after pumping at 980 nm in the 900-1150 nm region. (d), (e) Thermometric parameters for the physiologic scope. Dots are the experimental amounts from the Δ parameter gained of the spectra in (c).

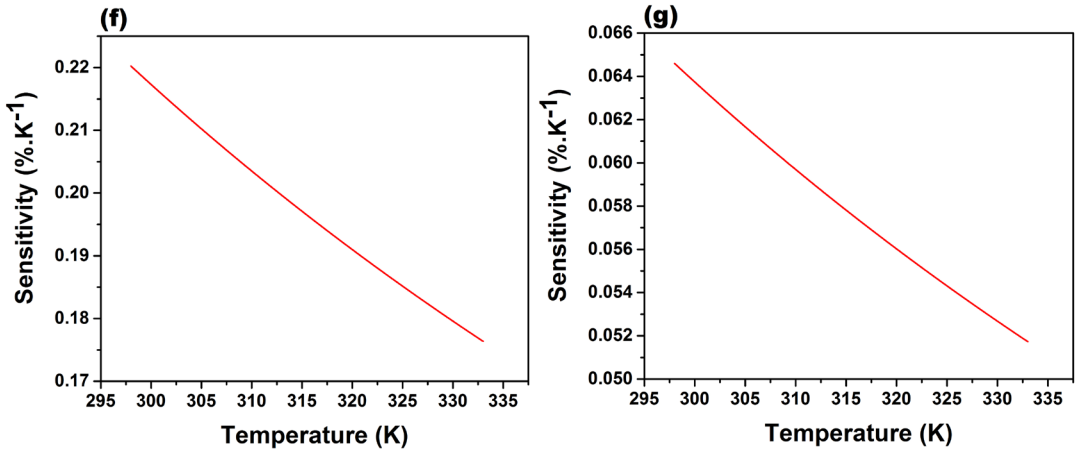

Figure 3.11. (f) Relative sensitivity of (d) in the physiologic scope. (g) Relative sensitivity of (e) in the physiologic scope.

CHAPTER 4. CONCLUSIONS

In this thesis, the luminescence properties of Yb^{3+}:YAG nanocrystals to suggest an absolute luminescent thermometer in that the calibration factor can be computed through the Yb^{3+} emission spectra in a certain composite were investiged. Yb^{3+}:YAG nanocrystals were synthesized by the sol-gel modified Pechini method and three routes of synthesis of Yb^{3+}:$Y_3Al_5O_{12}$ nanoparticles using the different metal precursors, the complexity agents, and the calcination temperature were done.

The crystallinity of the synthesized nanoparticles were characterized at room temperature exploiting X-ray diffraction (XRD) and after the comparing of the registered XRD pattern with the JCPDS database, the crystalline phases of Yb^{3+}:YAG nanocrystals were obtained.

The analyzing of the particle morphology and size distribution of the nanoparticles was accomplished utilizing transmission electron microscopy (TEM) examination, executed with a JEOL JEM-1011 microscope. By looking at the TEM images, the Yb^{3+}:YAG nanoparticles which were synthesized using EDTA (Figure 3.6f) were larger in comparison with those which were synthesized using citric acid (Figure 3.6g). A large degree of agglomeration among the nanoparticles were seen simultaneously in TEM images.

After testing the all synthesized nanoparticles using the absolute intensity technique, Exp. 10 nanocrystals of Yb^{3+}:YAG which were synthesized using $Y(NO_3)_3.6H_2O$ (Alfa Aesar, 99.9%), $Yb(NO_3)_3.5H_2O$ (Aldrich, 99.9%), and $Al(NO_3)_3.9H_2O$ (Sigma-Aldrich, 98%) as starting materials and citric acid as a complexing agent were shown the highest absolute emission intensity. Therefore, they were the best nanocrystals for our goal.

As a result, we reported the temperature sensing capabilities of 5 at. % Yb^{3+}:YAG nanoparticles as a novel contactless and non-invasive absolute luminescent nano-thermometer using the FIR technique. Under excitation at 940 nm and 980 nm, these nanoparticles showed emission bands at 1030, 1048, 1000, and 1006 nm within the near-infrared area of the spectrum, correlating with the $0' \rightarrow 2$, $0' \rightarrow 3$, $1' \rightarrow 3$, and $1' \rightarrow 2$ transitions of Yb^{3+}, and locating in the second biologic windows (II-BW), correspondingly. Therefore, emissions from both of these excitations displayed promising traits in order to the thermic detecting in this scope of wavelengths. Ergo, two different thermometric parameters were defined as the ratios for both of the excitations, first, the ratio betwixt the emission intensities of the $0' \rightarrow 2$ and $0' \rightarrow 3$ transitions corresponding to 1030 and 1048 nm peaks, second, the ratio betwixt the emission intensities of the $1' \rightarrow 3$ and $1' \rightarrow 2$ transitions referring to 1000 and 1006 nm peaks. The thermometer depends on the straightforward Yb^{3+} energy level diagram and be able to work betwixt 298 and 333 K with achieving quite low thermal sensitivities, 0.236 – 0.188 % K^{-1} and 0.109 – 0.087 % K^{-1} under excitation at 940 nm and 0.220 – 0.176 % K^{-1} and 0.0646 – 0.0517 % K^{-1} under excitation at 980 nm. The computing of the calibration factor through the Yb^{3+} emission spectra is the other recent and of outstanding significance perspective.

REFERENCES

[1] Mehta, V. K., Mehta, R., S. Chand's Principles of physics for class XI, S. Chand Publishing, 917-919.

[2] Childs, P.R.N., Greenwood, R.J., Long, C.A., Review of temperature measurement, Rev. Sci. Instrum., 71(8): 2959-2978, 2000.

[3] Wang, X.-D., Wolfbeis, O.S., Meier, R.J., Luminescent probes and sensors for temperature, Chem. Soc. Rev., 42(19): 7834-7869, 2013.

[4] Souza, A. S., Nunes, L.A.O., Silva, I.G.N., Oliveira, F.A.M., da Luz, L.L., Brito, H.F., Felinto, M.C.F.C., Ferreira, R.A.S., Júnior, S.A., Carlos, L.D., Malta, O.L., Highly-sensitive Eu^{3+} ratiometric thermometers based on excited state absorption with predictable calibration, Nanoscale, 8(9): 5327-5333, 2016.

[5] Brites, C.D.S., Lima, P.P., Silva, N.J.O., Millán, A., Amaral, V.S., Palacio, F., Carlos, L.D., Thermometry at the nanoscale, Nanoscale, 4(16): 4799-4829, 2012.

[6] Sole, J.G., Bausa, L.E., Jaque, D., An introduction to the optical spectroscopy of inorganic solids, West Sussex: John Wiley & Sons, 16-17, 2005.

[7] http://micro.magnet.fsu.edu/primer/java/jablonski/jabintro/index.html Access Date: 14.10.2017.

[8] Jaque, D., Vetrone, F., Luminescence nanothermometry, Nanoscale, 4(15): 4301-4326, 2012.

[9] http://www.nanothermometers.org/introduction/ Access Date: 27.10.2017.

[10] Pudovkin, M.S., Morozov, O.A., Pavlov, V.V., Korableva, S.L., E.V., Lukinova, Osin, Y.N., Evtugyn, V.G., Safiullin, R.A., Semashko, V.V., Physical Background for Luminescence Thermometry Sensors Based on Pr^{3+}:LaF_3 Crystalline Particles, Journal of Nanomaterials, Volume 2017, Article ID 3108586, 9 pages.

[11] Wade, S.A., Collins, S.F., Baxter, G.W., Fluorescence intensity ratio technique for optical fiber point temperature sensing, J. Appl. Phys., 94(8): 4743-4756, 2003.

[12] Jaque, D., del Rosal, B., Rodríguez, E.M., Maestro, L.M., Haro-González, P., Solé, J.G., Fluorescent nanothermometers for intracellular thermal sensing, Nanomedicine, 9(7): 1047-1062, 2014.

[13] Ekimov, A.I., Onushchenko, A.A., Quantum size effect in three-dimensional microscopic semiconductor crystals, Pis' ma Zh. Eksp. Teor. Fiz., 34(6): 363-366, 1981.

[14] Yu, W.W., Chang, E., Drezek, R., Colvin, V.L., Water-soluble quantum dots for biomedical applications, Biochemical and Biophysical Research Communications, 348(3): 781-786, 2006.

[15] http://www.sigmaaldrich.com/technical-documents/articles/materials science/nanomaterials/quantum-dots.html Access Date: 29.10.2017.

[16] Michalet, X., Pinaud, F.F., Bentolila, L.A., Tsay, J.M., Doose, S., Li, J.J., Sundaresan, G., Wu, A.M., Gambhir, S.S., Weiss, S., Quantum Dots for Live Cells, in Vivo Imaging, and Diagnostics, Science, 307(5709): 538-544, 2005.

[17] Medintz, I.L., Uyeda, H.T., Goldman, E.R., Mattoussi, H., Quantum dot bioconjugates for imaging, labelling and sensing, Nature materials, 4, 435-446, 2005.

[18] Walker, G.W., Sundar, V.C., Rudzinski, C.M., Wun, A.W., Bawendi, M. G., Nocera, D.G., Quantum-dot optical temperature probes, Appl. Phys. Lett, 83(17): 3555-3557, 2003.

[19] Han, B., Hanson, W.L., Bensalah, K., Tuncel, A., Stern, J.M., Cadeddu, J.A., Development of quantum dot-mediated fluorescence thermometry for thermal therapies, Ann. Biomed. Eng., 37(6): 1230-1239, 2009.

[20] Vlaskin, V.A., Janssen, N., van Rijssel, J., Beaulac, R., Gamelin, D.R., Tunable dual emission in doped semiconductor nanocrystals, Nano Lett., 10(9): 3670-3674, 2010.

[21] MacLaurin, E.J., Vlaskin, V.A., and Gamelin, D.R., Water-soluble dualemitting nanocrystals for ratiometric optical thermometry, J. Am. Chem. Soc., 133(38): 14978-14980, 2011.

[22] Hsia, C.H., Wutting, A., and Yang, H., An accessible approach to preparing water-soluble Mn^{2+}-doped (CdSSe) ZnS (core) shell nanocrystals for ratiometric temperature sensing, ACS Nano, 5(12): 9511-9522, 2011.

[23] van Sark, W.G.J.H.M., Frederix, P.L.T.M., Bol, A.A., Gerritsen, H.C., Meijerink, A., Blueing, Bleaching, and Blinking of Single CdSe/ZnS Quantum Dots, ChemPhysChem, 3(10): 871-879, 2002.

[24] Isnaeni, Kim, K.H., Nguyen, D.L., Lim, H., Nga, P.T., Cho, Y.H., Appl. Phys. Lett., Shell layer dependence of photoblinking in CdSe/ZnSe/ZnS quantum dots, 98(1): 012109-012112, 2011.

[25] Nakamura, M., Ozaki, S., Abe, M., Matsumoto, T., Ishimura, K., One-pot synthesis and characterization of dual fluorescent thiol-organosilica nanoparticles as non-photoblinking quantum dots and their applications for biological imaging, J. Mater. Chem., 21(12): 4689-4695, 2011.

[26] Cho, S.J., Maysinger, D., Jain, M., Roder, B., Hackbarth, S., Winnik, F.M., Long-Term Exposure to CdTe Quantum Dots Causes Functional Impairments in Live Cells, Langmuir, 23(4): 1974-1980, 2007.

[27] Gnach, A., Lipinski, T., Bednarkiewicz, A., Rybka, J., Capobianco, J.A., Upconverting nanoparticles: assessing the toxicity, Chem. Soc. Rev., 44(6): 1561-1584, 2015.

[28] Malik A., Grohmann, E., Dyes-environmental impact and remediation. In: Environmental protection strategies for sustainable development, Strategies for sustainability, Springer, 111-162, 2012.

[29] S., Garfield, Mauve: how one man invented a color that changed the world (NewYork: W. W. Norton & Company), 2002.

[30] Ross, D., Gaitan, M., Locascio, L.E., Temperature Measurement in Microfluidic Systems Using a Temperature-Dependent Fluorescent Dye, Anal. Chem., 73(17): 4117-4123, 2001.

[31] Guan, X., Liu, X., Su, Z., Preparation and photophysical behaviors of fluorescent chitosan bearing fluorescein: Potential biomaterial as temperature/pH probes, J. Appl. Polym. Sci., 104(6): 3960-3966, 2007.

[32] Mikkelsen, R.B., Wallach, D.F.H., Temperature sensitivity of the erythrocyte membrane potential as determined by cyanine dye fluorescence, Cell Biol. Int. Rep., 1(1): 51-55, 1977.

[33] Löw, P., Kim, B., Takama, N., Bergaud, C., High-spatial-resolution surfacetemperature mapping using fluorescent thermometry, Small, 4(7): 908-914, 2008.

[34] Ebert, S., Travis, K., Lincoln, B., Guck, J., Fluorescence ratio Thermometry in a microfluidic dual-beam laser trap, Opt. Express, 15(23): 15493-15499, 2007.

[35] Peterman, E.J.G., Gittes, F., Schmidt, C.F., Laser-induced heating in optical traps, Biophys. J., 84(2): 1308-1316, 2003.

[36] Bennet, M.A., Richardson, P.R., Arlt, J., McCarthy, A., Buller, G.S., Jones, A.C., Optically trapped microsensors for microfluidic temperature measurement by fluorescence lifetime imaging microscopy, Lab Chip, 11(22): 3821-3828, 2011.

[37] Mendels, D.-A., Graham, E.M., Magennis, S.W., Jones, A.C., Mendels, F., Quantitative comparison of thermal and solutal transport in a T-mixer by FLIM and CFD, Microfluid. Nanofluid., 5(5): 603-617, 2008.

[38] http://www.essentialchemicalindustry.org/polymers/polymers-an-overview.html Access Date: 30.10.2017.

[39] Yang, J., Bai, F., Temperature dependence of the fluorescence spectra of ladderlike polyphenylsilsesquioxane and ladderlike 1,4-phenylene-bridged polyvinylsiloxane, Chin. J. Polym. Sci., 20, 15-23, 2002.

[40] Uchiyama, S., Kawai, N., de Silva, A.P., Iwai, K., Fluorescent polymeric AND logic gate with temperatura and pH as inputs, J. Am. Chem. Soc., 126(10): 3032-3033, 2004.

[41] Uchiyama, S., Matsumura, Y., de Silva, A.P., Iwai, K., Fluorescent molecular thermometers based on polymers showing temperature-induced phase transitions and labeled with polarity-responsive benzofurazans, Anal. Chem., 75(21): 5926-5935, 2003.

[42] Graham, E.M., Iwai, K., Uchiyama, S., de Silva, A.P., Magennis, S.W., Jones, A.C., Quantitative mapping of aqueous microfluidic temperature with sub-degree resolution using fluorescence lifetime imaging microscopy, Lab Chip, 10(10): 1267-1273, 2010.

[43] Okabe, K., Inada, N., Gota, C., Harada, Y., Funatsu, T., Uchiyama, S., Intracellular temperature mapping with a fluorescent polymeric thermometer and fluorescence lifetime imaging microscopy, Nat. Commun., 3(705): 1-9, 2012.

[44] Gota, C., Okabe, K., Funatsu, T., Harada, Y., Uchiyama, S., Hydrophilic Fluorescent Nanogel Thermometer for Intracellular Thermometry, J. Am. Chem. Soc., 131(8): 2766-2767, 2009.

[45] Yang, D., Ma, P., Hou, Z., Cheng, Z., Li, C., Lin, J., Current advances in lanthanide ion (Ln^{3+})-based upconversion nanomaterials for drug delivery, Chem. Soc. Rev., 44(6): 1416-1448, 2015.

[46] Imbusch, G.F., Henderson, B., Optical Spectroscopy of Inorganic solids, London: Oxford Science Publications, 2006.

[47] Yap, S.V., Ranson, R.M., Cranton, W.M., Koutsogeorgis, D.C., Hix, G.B., Temperature dependent characteristics of La_2O_2S: Ln [Ln=Eu, Tb] with various Ln concentrations over 5–60 °C, J. Lumin., 129(5): 416-422, 2009.

[48] Haro-Gonzalez, P., Martin, I.R., Martin, L.L., Leon-Luis, S.F., Perez-Rodriguez, C., Lavin, V., Characterization of Er^{3+} and Nd^{3+} doped strontium barium niobate glass ceramic as temperature sensors, Opt. Mater., 33(5): 742-745, 2011.

[49] Brites, C.D.S., Lima, P.P., Silva, N.J.O., Millan, A., Amaral, V.S., Palacio, F., Carlos, L.D.A., Luminescent molecular thermometer for long-term absolute temperatura measurements at the nanoscale, Adv. Mater., 22(40): 4499-4504, 2010.

[50] Benayas, A., Escuder, E., Jaque, D., High-resolution confocal fluorescence thermal imaging of tightly pumped microchip Nd:YAG laser ceramics, Appl. Phys. B: Lasers Opt., 107(3): 697-701, 2012.

[51] Yu, J., Sun, L., Peng, H., Stich, M.I.J., Luminescent terbium and europium probes for lifetime based sensing of temperature between 0 and 70 °C, J. Mater. Chem., 20: 6975-6981, 2010.

[52] Haase, M., Schäfer, H., Upconverting nanoparticles, Angew. Chem. Int. Ed., 50(26): 5808-5829, 2011.

[53] Mader, H.S., Kele, P., Saleh, S.M., Wolfbeis, O.S., Upconverting luminescent nanoparticles for use in bioconjugation and bioimaging, Current Opinion in Chemical Biology, 14(5): 582-596, 2010.

[54] Zeng, X., Zhao, Z., Zhao, G., He, X., Xu, X., Pang, H., Li, H., Jie, M.Y., Xu, J., Yan, C., Comparison of spectroscopic parameters of 15 at % Yb: $YAlO_3$ and 15 at % Yb:$Y_3Al_5O_{12}$, Journal of Crystal Growth, 274(1-2): 106-112, 2005.

[55] Wang, X., Xu, X., Zeng, X., Zhao, Z., Jiang, B., He, X., Xu, J., Effects of Yb concentration on the spectroscopic properties of Yb:$Y_3Al_5O_{12}$, Spectrochimica Acta Part A, 63(1): 49-54, 2006.

[56] DeLoach, L.D., Payne, S.A., Chase, L.L., Smith, L.K., Kway, W.L., Krupke, W.F., Evaluation of Absorption and Emission Properties of Yb^{3+} Doped Crystals for Laser Applications, IEEE JOURNAL OF QUANTUM ELECTRONICS, 29(4): 1179-1191, 1993.

[57] Xu, X., Zhao, Z., Song, P., Zhou, G., Xu, J., Deng, P., Structural, thermal, and luminescent properties of Yb-doped $Y_3Al_5O_{12}$ crystals, J. Opt. Soc. Am. B, 21(3): 543-547, 2004.

[58] Boulon, G., Why so deep research on Yb^{3+}-doped optical inorganic materials?, Journal of Alloys and Compounds, 451(1-2): 1-11, 2008.

[59] https://en.wikipedia.org/wiki/Yttrium_aluminium_garnet
Access Date: 25.10.2017.

[60] Wright, J., Guceri, S., Gogotsi, Y.G., Kuznetsov, V., Nanoengineered nanofibrous materials, Springer Science & Business Media, 436-437, 2007.

[61] Strek, W., Marciniak, L., Gluchowski, P., Hreniak, D., Infrared laser stimulated broadband white emission of Yb^{3+}:YAG nanoceramics, Optical Materials, 35(11): 2013-2017, 2013.

[62] Xie, R.J., Li, Y.Q., Hirosaki, N., Yamamoto, H., Nitride phosphors and solid-state lighting, CRC Press, 77-78, 2016.

[63] https://en.wikipedia.org/wiki/Crystallographic_point_group#cite_note-1
Access Date: 22.10.2017.

[64] https://en.wikipedia.org/wiki/List_of_space_groups
Access Date: 22.10.2017.

[65] http://scripts.iucr.org/cgi-bin/sendcif?oh0057sup2
Access Date: 22.10.2017.

[66] Zafarullah, I., Thulium ions in a yttrium aluminum garnet host for quantum computing applications: material analysis and single qubit operations, Montana State University, Department of Physics, Doctor of Philosophy Thesis, 62-63, 2008.

[67] Veith, M., Mathur, S., Kareiva, A., Jilavi, M., Zimmer, M., Huch, V., Low temperature synthesis of nanocrystalline $Y_3Al_5O_{12}$ (YAG) and Ce-doped $Y_3Al_5O_{12}$ via different sol-gel methods, J. Mater. Chem., 9, 3069-3079, 1999.

[68] Wang, H. M., Simmonds, M. C., Huang, Y. Z., Rodenburg, J. M., Synthesis of nanosize powders and thin films of Yb-doped YAG by sol-gel methods, Chem. Mater., 15(18): 3474-3480, 2003.

[69] Garskaite, E., Lindgren, M., Einarsrud, M.-A., Grande, T., Luminescent properties of rare earth (Er, Yb) doped yttrium aluminium garnet thin films and bulk samples synthesised by an aqueous sol–gel technique, Journal of the European Ceramic Society, 30(7): 1707-1715, 2010.

[70] Levy, D., Zayat, M., The Sol-Gel Handbook: Synthesis, Characterization and Applications, 3-Volume Set, John Wiley & Sons, 2015.

[71] Theodore, L., Nanotechnology: Basic Calculations for Engineers and Scientist, John Wiley & Sons, 233-235, 2006.

[72] Pechini, M.P., Method of preparing lead and alkaline earth titanates and niobates and coating method using the same to form a capacitor. US patent 3330697, 1967.

[73] Galceran, M., Pujol, M.C., Aguiló, M., Díaz, F., Sol-gel modified Pechini method for obtaining nanocrystalline $KRE(WO_4)_2$(RE = Gd and Yb), Journal of Sol-Gel Science and Technology, 42(1): 79-88, 2007.

[74] Xu, Y., Ming Chen, X., Jun Wu, Y., Preparation of $Ba_{6-3x}Nd_{8+2x}Ti_{18}O_{54}$ via Ethylenediaminetetraacetic Acid Precursor, J. Am Ceram. Soc., 83(11): 2893-2995, 2000.

[75] https://en.wikipedia.org/wiki/X-ray_crystallography
Access Date: 24.10.2017.

[76] Stanjek, H., Häusler, W., Basics of X-ray Diffraction, Hyperfine Interactions, 154:107-119, 2004.

[77] http://www.ammrf.org.au/myscope/xrd/practice/prep/#prettyPhoto.
Access Date: 06.10.2017.

[78] http://www.icdd.com/profile/overview.htm Access Date: 06.10.2017.

[79] Hawkes, P.W., Ernst Ruska, Phys. Today, 43, 84-85, 1990.

[80] https://en.wikipedia.org/wiki/Electron_microscope
Access Date: 22.10.2017.

[81] https://en.wikipedia.org/wiki/Luminescence Access Date: 24.10.2017.

[82] Solé, J.G., Bausá, L.E., Jaque, D., An Introduction to the Optical Spectroscopy of Inorganic Solids, West Sussex: John Wiley and Sons, 2005.

[83] J.-C., Boyer, van Veggel, F.C.J.M., Absolute quantum yield measurements of colloidal $NaYF_4:Er^{3+}$, Yb^{3+} upconverting nanoparticles, Nanoscale, 2: 1417-1419, 2010.

[84] Amami, J., Hreniak, D., Guyot, Y., Zhao, W., Boulon, G., Size-effect on concentration quenching in Yb^{3+}-doped $Y_3Al_5O_{12}$ nano-crystals, Journal of Luminescence, 130(4): 603-610, 2010.

[85] Monshi, A., Froughi, M.R., Monshi, M.R., Modified Scherrer Equation to Estimate More Accurately Nano-Crystallite Size Using XRD, J. Nano Sci Eng., 2: 154-160, 2012.

[86] Alexander, L., Klug, H.P., Determination of Crystallite Size with the X-Ray Spectrometer, J. Appl.Phys., 21(2): 137-143, 1950.

[87] https://en.wikipedia.org/wiki/Full_width_at_half_maximum
Access Date: 24.10.2017.

[88] Galceran, M., Pujol, M.C., Carvajal, J.J., Tkaczyk, S., Kityk, I.V., Díaz, F., Aguiló, M., Synthesis and characterization of $KTiOPO_4$ nanocrystals and their PMMA nanocomposites, Nanotechnology, 20(3): 1-10, 2008.

[89] Ferreira, J., Santos, L.F., Almeida, R.M., Sol–gel-derived Yb:YAG polycrystalline ceramics for laser applications, Journal of Sol-Gel Science and Technology, 83(2): 436-446, 2017

[90] Xua, X., Zhaoa, Z., Song, P., Jiang, B., Zhou, G., Xu, J., Deng, P., Bourdet, G., Chanteloup, J.C., Zou, J.-P., Fulop, A., Upconversion luminescence in Yb^{3+}-doped yttrium aluminum garnets, Physica B, 357(3-4): 365-369, 2005.

[91] Luo, D., Zhang, J., Xu, C., Qin, X., Tang, D., Ma, J., Fabrication and laser properties of transparent Yb:YAG ceramics, Optical Materials, 34(6): 936-939, 2012.

[92] Tang, F., Cao, Y., Guo, W., Chen, Y., Huang, J., Deng, Z., Liu, Z., Huang, Z., Fabrication and laser behavior of the Yb:YAG ceramic microchips, Optical Materials, 33(8): 1278-1282, 2011.

[93] Tang, F., Cao, Y., Huang, J., Liu, H., Guo, W., Wang, W., Fabrication and Laser Behavior of Composite Yb:YAG Ceramic, Journal of the American Ceramic Society, 95(1): 56-59, 2012.

ANNEX

Annex A: Crystallographic Information File (CIF) of YAG

```
_chemical_formula_moiety     ?
_chemical_formula_sum     'Al5 O12 Y3'
_chemical_formula_weight     593.613
_symmetry_cell_setting     cubic
_symmetry_space_group_name_H-M     'I a -3 d'
_symmetry_space_group_name_Hall     '-I 4bd 2ab 3'
loop_
    _symmetry_equiv_pos_as_xyz
    'x,y,z'
    '1/2+x,y,1/2-z'
    'x,1/2-y,1/2+z'
    '1/2-x,1/2+y,z'
    '-z,-x,-y'
    '1/2-z,1/2+x,y'
    '1/2+z,x,1/2-y'
    'z,1/2-x,1/2+y'
    '-y,-z,-x'
    'y,1/2-z,1/2+x'
    '1/2-y,1/2+z,x'
    '1/2+y,z,1/2-x'
    '1/4-y,3/4-x,3/4+z'
    '1/4+y,1/4+x,1/4+z'
    '3/4-y,3/4+x,1/4-z'
    '3/4+y,1/4-x,3/4-z'
    '1/4-x,3/4-z,3/4+y'
    '3/4+x,1/4-z,3/4-y'
    '1/4+x,1/4+z,1/4+y'
    '3/4-x,3/4+z,1/4-y'
    '1/4-z,3/4-y,3/4+x'
    '3/4-z,3/4+y,1/4-x'
    '3/4+z,1/4-y,3/4-x'
    '1/4+z,1/4+y,1/4+x'
    '-x,-y,-z'
    '1/2-x,-y,1/2+z'
    '-x,1/2+y,1/2-z'
    '1/2+x,1/2-y,-z'
    'z,x,y'
    '1/2+z,1/2-x,-y'
    '1/2-z,-x,1/2+y'
    '-z,1/2+x,1/2-y'
    'y,z,x'
    '-y,1/2+z,1/2-x'
    '1/2+y,1/2-z,-x'
    '1/2-y,-z,1/2+x'
```

'3/4+y,1/4+x,1/4-z'
'3/4-y,3/4-x,3/4-z'
'1/4+y,1/4-x,3/4+z'
'1/4-y,3/4+x,1/4+z'
'3/4+x,1/4+z,1/4-y'
'1/4-x,3/4+z,1/4+y'
'3/4-x,3/4-z,3/4-y'
'1/4+x,1/4-z,3/4+y'
'3/4+z,1/4+y,1/4-x'
'1/4+z,1/4-y,3/4+x'
'1/4-z,3/4+y,1/4+x'
'3/4-z,3/4-y,3/4-x'
'1/2+x,1/2+y,1/2+z'
'x,1/2+y,-z'
'1/2+x,-y,z'
'-x,y,1/2+z'
'1/2-z,1/2-x,1/2-y'
'-z,x,1/2+y'
'z,1/2+x,-y'
'1/2+z,-x,y'
'1/2-y,1/2-z,1/2-x'
'1/2+y,-z,x'
'-y,z,1/2+x'
'y,1/2+z,-x'
'3/4-y,1/4-x,1/4+z'
'3/4+y,3/4+x,3/4+z'
'1/4-y,1/4+x,3/4-z'
'1/4+y,3/4-x,1/4-z'
'3/4-x,1/4-z,1/4+y'
'1/4+x,3/4-z,1/4-y'
'3/4+x,3/4+z,3/4+y'
'1/4-x,1/4+z,3/4-y'
'3/4-z,1/4-y,1/4+x'
'1/4-z,1/4+y,3/4-x'
'1/4+z,3/4-y,1/4-x'
'3/4+z,3/4+y,3/4+x'
'1/2-x,1/2-y,1/2-z'
'-x,1/2-y,z'
'1/2-x,y,-z'
'x,-y,1/2-z'
'1/2+z,1/2+x,1/2+y'
'z,-x,1/2-y'
'-z,1/2-x,y'
'1/2-z,x,-y'
'1/2+y,1/2+z,1/2+x'
'1/2-y,z,-x'
'y,-z,1/2-x'
'-y,1/2-z,x'
'1/4+y,3/4+x,3/4-z'
'1/4-y,1/4-x,1/4-z'
'3/4+y,3/4-x,1/4+z'
'3/4-y,1/4+x,3/4+z'
'1/4+x,3/4+z,3/4-y'
'3/4-x,1/4+z,3/4+y'
'1/4-x,1/4-z,1/4-y'
'3/4+x,3/4-z,1/4+y'
'1/4+z,3/4+y,3/4-x'
'3/4+z,3/4-y,1/4+x'
'3/4-z,1/4+y,3/4+x'

```
    '1/4-z,1/4-y,1/4-x'
_cell_length_a     12.0062(5)
_cell_length_b     12.0062(5)
_cell_length_c     12.0062(5)
_cell_angle_alpha     90.0
_cell_angle_beta     90.0
_cell_angle_gamma     90.0
_cell_volume     1730.7(2)
_cell_formula_units_Z     8
_cell_measurement_reflns_used     25
_cell_measurement_theta_min     22.5
_cell_measurement_theta_max     25.0
_cell_measurement_temperature     296
_exptl_crystal_description     'sphere'
_exptl_crystal_colour     ?
_exptl_crystal_size_max     ?
_exptl_crystal_size_mid     ?
_exptl_crystal_size_min     ?
_exptl_crystal_size_rad      .095
_exptl_crystal_density_diffrn     4.56
_exptl_crystal_density_meas     ?
_exptl_crystal_F_000     2224
_exptl_absorpt_coefficient_mu     21.21
_exptl_absorpt_correction_type     'spherical'
_exptl_absorpt_correction_T_min     ?
_exptl_absorpt_correction_T_max     ?
_diffrn_radiation_type     'MoK\a'
_diffrn_radiation_wavelength      .71069
_diffrn_measurement_device     'Rigaku AFC-6'
_diffrn_measurement_method     '\w-2\q'
_diffrn_reflns_number     3294
_diffrn_reflns_av_R_equivalents      .019
_diffrn_reflns_theta_max     60
_diffrn_reflns_limit_h_min     ?
_diffrn_reflns_limit_h_max     ?
_diffrn_reflns_limit_k_min     ?
_diffrn_reflns_limit_k_max     ?
_diffrn_reflns_limit_l_min     ?
_diffrn_reflns_limit_l_max     ?
_diffrn_standards_number     ?
_diffrn_standards_interval_count     ?
_diffrn_standards_interval_time     ?
_diffrn_standards_decay_%     ?
_reflns_number_total     ?
_reflns_number_observed     294
_reflns_observed_criterion     |F~o~|>3\s(|F~o~|)
_refine_ls_structure_factor_coef     F
_refine_ls_R_factor_obs      .029
_refine_ls_wR_factor_obs      .026
_refine_ls_goodness_of_fit_obs     ?
_refine_ls_number_reflns     294
_refine_ls_number_parameters     ?
_refine_ls_hydrogen_treatment     ?
_refine_ls_weighting_scheme     '1/\s^2^(F~o~)'
_refine_ls_shift/esd_max     ?
_refine_diff_density_max     ?
_refine_diff_density_min     ?
_refine_ls_extinction_method     ?
_refine_ls_extinction_coef     ?
```

```
_atom_type_scat_source      'IntTabIV'
loop_
    _atom_site_label
    _atom_site_fract_x
    _atom_site_fract_y
    _atom_site_fract_z
    Y   .125   .0   .25
    Al1   .0   .0   .0
    Al2   .375   .0   .25
    O   -.0318(3)   .0511(3)   .1498(3)
```

Annex B: The Synthesized Yb^{3+}-doped YAG Nanoparticles Different Colors

White | Celadon | Grey-White | Brown | Yellowish

RESUME

Hossein EBRAHIM HOSSEINI TAZEH KANDI was born on March 3rd, in 1988 in Marand which is located in Islamic Republic of Iran. He completed his elementary, middle, and high school educations in Marand. He graduated from Bahman Shamlou 1 high School in Mathematics and Physics in 2005 and earned his university-preparatory school's diploma from Shahid Dr. Beheshti prep school in 2006. He started his bachelor program in the field of Physics (Solid State) at Payame Noor University in 2007 in Marand and gained his bachelor diploma after completing his program on February 19th, 2011. Because of his interest to Nanoscience field, he applied to Nanoscience and Nanoengineering program in Sakarya University in 2015 as his master program. He participated in the Turkey Erasmus Programme and Erasmus+ in Sakarya University. Then, he went to Rovira i Virgili (URV), which is located in Tarragona in Spain, as an exchange student after passing the English exam. He joind to Química Física i Inorganica Física i Cristal•lografia de Materials i Nanomaterials (FiCMA-FiCNA) group of the Departament de Química Física i Inorganica of the Universitat Rovira i Virgili and started his investigation on Yb^{3+}:YAG nanocrystals as a nanothermometer on September 1st, 2016. Currently, he is going to continue his education in Ph.D.